University of Zurich[UZH]

Quantifying the effect of non-linear memory on the tests of general relativity with gravitational waves observations

Master Thesis in Physics

Parisa Rezaei Mianroodi

Supervised by
Prof. Dr. Philippe Jetzer
Dr. Shubhanshu Tiwari

April 24, 2023

Abstract

In the first chapter of this work, we note some rather general information about the nature of gravitational waves (GW) which is then followed by presenting recent results of observing them using GW detectors. And finally, a short theoretical introduction to non-linear memory caused by passage of GW. Then in chapter 2, we go into more detail about the properties of gravitational waves by studying the evolution of binary black hole systems. We present different formalism to simulate this evolution and generate wave forms. Then we study the effect of different parameters of the system such as mass ratio or spin on the wave form. Chapter3 is solely devoted to non-linear memory and its dependence on different source parameter. In chapter 4, we talk about inference of source parameter. We introduce some concepts such as match and signal-to-noise ratio. We investigate degeneracies in BBH source parameters. The main result of this work comes in chapter 5, where we study effect of non-linear memory on parameterized test of GR by generating different plots that demonstrates the match between the wave forms generated solely by GR simulations while taking non-linear memory into account and wave forms generated by beyond GR simulation formalism. Finally, chapter 6 summarises the result.

Acknowledgements

First and foremost, I am grateful to Philippe Jetzer, who gave me the opportunity to discover and gain priceless insight into one of his fascinating research fields through this work.

I would like to thank Shubhanshu Tiwari, for all his continuous support and patience during my master thesis. His immense knowledge and experience has helped me in each and every step of this work. The door to his office was always open whenever I had a question or faced a problem throughout literature reading, coding and writing.

Sincere thanks also to Emanuel Hänsenberger, whose moral support was a great help for me to overcome any kind of obstacles. And at last, I'd like to thank my family who always believed in me to this day.

Contents

1 Introduction **1**
- 1.1 Gravitational Waves detectors . . . 5
- 1.2 Recent results . . . 9
- 1.3 Non-linear memory . . . 11

2 Properties of gravitational waves emitted from binary black holes **14**
- 2.1 Evolution of binary black hole system . . . 14
  - 2.1.1 Post-Newtonian formalism . . . 16
  - 2.1.2 Perturbation theory gravitational self force . . . 18
  - 2.1.3 Numerical relativity . . . 19
  - 2.1.4 Effective one body formalism . . . 20
  - 2.1.5 Order of magnitude . . . 20
- 2.2 Examples of BBH evolutions . . . 21
  - 2.2.1 Effect of mass ratio . . . 21
  - 2.2.2 Effect of aligned spin . . . 22
  - 2.2.3 Effect of misaligned spin (Precession) . . . 23

3 Non-linear memory **27**
- 3.1 Dependence of non-linear memory on total mass . . . 31
- 3.2 Dependence of non-linear memory on mass-ratio . . . 33
- 3.3 Dependence of non-linear memory on Aligned spins . . . 34
- 3.4 Dependence of memory on inclination angle . . . 35

4 Inference of source parameters from BBH detectors **36**
- 4.1 Signal to noise ratio (SNR) . . . 38
- 4.2 Match . . . 40
- 4.3 Degeneracies in BBH source parameters . . . 41
- 4.4 Mass-ratio spin degeneracy . . . 42

5 Effect of non-linear memory on test of GR **44**
- 5.1 Introduction to test of GR with gravitational wave Ligo/Virgo . 44
- 5.2 Parameterized test of General Relativity with Gravitational Waves 53
- 5.3 Effect of non-linear memory on test of general relativity . . . 55

5.3.1 Impact on generic parameterized test of GR 55
5.3.2 Impact on inspiral merger ringdown tests 58

6 Conclusions **60**

Chapter 1

Introduction

Gravitational waves (GW) are a direct consequence of general relativity which are generated by accelerated masses. They can be interpreted as the effect of the change of the gravitational field at one local region, on an observer far away in another region after a limited time. On September 9-th 2015, LIGO-Virgo detected GWs from merging binary black holes. Over a hundred years ago, Einstein found out that gravitational waves are a solution of the linearized field equations, which can be described by finding a solution by linearly approximating the metric in a weak field regime.

We begin by adding the derivation of gravitational waves. The Einstein's Field Equation (EFE) is a relation between the space-time curvature and the mass, given by:

$$R_{\mu\nu} - \frac{1}{2} g_{\mu\nu} R = \frac{8\pi G}{4} T_{\mu\nu}, \tag{1.1}$$

where on the L.H.S $R_{\mu\nu}$ is the *Ricci curvature tensor*, R is the *Ricci scalar* and $g_{\mu\nu}$ is the metric on the space-time manifold $\mathcal{M}$. These quantities describes the space-time. While on the R.H.S $T_{\mu\nu}$ is the stress-energy tensor describing the matter distribution. G and c are gravitational constant and speed of light in vacuum respectively. Bianchi identity implies the local energy conservation if the equation (1.1) holds. Following general relativity textbook of R. Wald, the entire content of GR can be summarized as follows: Space-time is a manifold $\mathcal{M}$ on which there is defined a metric $g_{\mu\nu}$. The curvature of $g_{\mu\nu}$ is related to the matter distribution in space-time by equation (1.1).

Let's assume that the metric tensor $g_{\mu\nu}$ has the form of a slightly perturbed Minkowski metric $\eta_{\mu\nu} = diag\{-1, 1, 1, 1\}$,

$$g_{\mu\nu} = \eta_{\mu\nu} + \epsilon\kappa_{\mu\nu}, \tag{1.2}$$

where $0 < \epsilon \ll 1$ (Since there is no natural positive definite metric on space-time, there is no natural norm by which "smallness" can be measured. An adequate definition of small is hence only the space-like components of $\epsilon\kappa_{\mu\nu}$

be much smaller than 1 in some global inertial coordinate system of $\eta_{\mu\nu}$). We consider the *linear approximation*, by which we simply mean that if we develop the L.H.S of equation (1.1) in the powers of ϵ, we neglect all the terms involving ϵ^k with $k > 1$. This formulation of GR is referred to as *linearized gravity*. In linearized gravity, indices can be raised and lowered by using $\eta_{\mu\nu}$. We call the quantity $h_{\mu\nu} = \epsilon\kappa_{\mu\nu}$, the *perturbation metric* (or perturbation tensor). The connection $\Gamma^{\rho}_{\mu\nu}$ to the linear order in $h_{\mu\nu}$, can now be written as:

$$\Gamma^{\rho}_{\mu\nu} = \frac{1}{2}\eta^{\rho\sigma}(\partial_\nu h^{\rho}_{\mu} + \partial_\mu h^{\rho}_{\nu} - \partial^\rho h_{\mu\nu}). \tag{1.3}$$

And the Reimann tensor can be found out:

$$R^{\mu}_{\nu\rho\sigma} = \frac{1}{2}(\partial_\rho\partial_\nu h^{\mu}_{\sigma} + \partial_\sigma\partial^\mu h_{\nu\sigma} - \partial_\sigma\partial_\nu h^{\mu}_{\rho}), \tag{1.4}$$

which can be contracted to get the Ricci tensor:

$$R_{\mu\nu} = R^{\rho}_{\mu\nu\rho} = \frac{1}{2}(\partial_\rho\partial_\nu h_\mu + \partial^\rho\partial_\mu h_{\nu\rho} - h_{\mu\nu} - \partial_\mu\partial_\nu h), \tag{1.5}$$

where $h = h^{\mu}_{\mu}$ is the trace of the perturbation metric. We define $\Box = \partial^{\mu}_{\mu} = \partial_x + \partial_y + \partial_z - \partial_t$, also known as the D'alembertian operator. Further contraction of Ricci tensor leads to Ricci scalar:

$$R = R^{\mu}_{\mu} = (\partial_\nu\partial^\mu h^{\nu}_{\mu} - \Box h). \tag{1.6}$$

We have now all the ingredients for the space-time description. Often $G_{\mu\nu} \equiv R_{\mu\nu} - \frac{1}{2}g_{\mu\nu}R$ is called as the *Einstein Tensor* , we substitute all these components in the L.H.S. of equation (1.1):

$$G_{\mu\nu} = R_{\mu\nu} - \frac{1}{2}R\eta_{\mu\nu} \tag{1.7}$$

$$= \frac{1}{2}(\partial_\rho\partial_{nu}h^{\rho}_{\mu} + \partial^\rho\partial_\mu h_{\nu\rho} - \Box h_{\mu\nu} - \partial_\mu\partial_\nu h) - \eta_{\mu\nu}\partial_\rho\partial^\sigma h^{\rho}_{\sigma} + \eta_{\mu\nu}\Box h), \tag{1.8}$$

Which is greatly simplified in the trace reverse formalism of Landau-Lifshitz, where the perturbation is written as $\tilde{h}_{\mu\nu} = h_{\mu\nu} - \frac{1}{2}\eta_{\mu\nu}$,

$$G_{\mu\nu} = \frac{1}{2}(\partial_\rho\partial_{nu}\tilde{h}^{\rho}_{\mu} + \partial^\rho\partial_\mu\tilde{h}_{\nu\rho} - \Box\tilde{h}_{\mu\nu} - \eta_{\mu\nu}\partial_\rho\partial^\sigma\tilde{h}^{\rho}_{\sigma}). \tag{1.9}$$

Finally we can write the equation of the linearized gravity as:

$$\partial_\rho\partial_{nu}\tilde{h}^{\rho}_{\mu} + \partial^\rho\partial_\mu\tilde{h}_{\nu\rho} - \Box\tilde{h}_{\mu\nu} - \eta_{\mu\nu}\partial_\rho\partial^\sigma\tilde{h}^{\rho}_{\sigma} = \frac{16\pi G}{c^4}T_{\mu\nu}. \tag{1.10}$$

These equations are symmetric in two indices hence the gauge needs to be fixed to arrive at a solution, we apply the gauge called as *Lorentz gauge* (sometimes called as the *de Donder gauge* (sometimes as *harmonic gauge* (and sometimes *Hilbert gauge*))), defined as:

$$\partial^\mu\tilde{h}_{\mu\nu} = 0 \tag{1.11}$$

For the perturbation metric to satisfy this gauge, the following equation should be satisfied:

$$\Box\epsilon_\nu = \partial^\mu \tilde{h}_{\mu\nu} \tag{1.12}$$

where ϵ_ν is the arbitrary infinitesimal vector field, defining the general infinitesimal coordinate transform. The linearized equations in the Lorentz gauge becomes:

$$\Box\tilde{h}_{\mu\nu} = -\frac{16\pi G}{c^4} T_{\mu\nu} \tag{1.13}$$

and in vacuum its $\Box\tilde{h} = 0$. It can be noted that the Equation (1.13) admits a class of homogeneous solutions, which are superimposition of plane waves, given by:

$$\tilde{h}_{\mu\nu}(x,t) = \mathrm{Re}\int d^3k A_{\mu\nu} \exp^{ik_\mu x_\mu} \tag{1.14}$$

where $k_\mu = (\omega/c, \overrightarrow{k})$ and $x^\mu = (ct, \overrightarrow{x})$ are the wave and position vectors respectively.
The choice of using Lorentz gauge is the freedom to choose coordinates, one can choose any gauge but the equations will become more cumbersome as $\partial^\mu \tilde{h}_{\mu\nu} = 0$ will not be ensured. With other choice of gauge perhaps separating gauge effects from physical effects might not be easy. The gauge choice caused a lot of confusion for the first 30+ years after Einstein wrote his equations.

Metric perturbation had ten degrees of freedom, which got reduced to six in the Lorentz gauge. One can show that Lorentz gauge did not use up all the gauge freedom, because an infinitesimal change in the coordinate $\overline{x}^\alpha = x^\alpha + \epsilon^\alpha$ preserves the gauge if $\partial_\beta \epsilon^{\alpha\beta} = 0$. This freedom indicates that there is still some residual gauge freedom left, which can be used to further simplify the solutions to the wave equations. Hence we can additionally demand our solution to be trace-less and transverse, this is unsurprisingly called the transverse-trace less (TT) gauge (for details see the lectures of Schutz and Ricci [1]). After the application of TT gauge, no more gauge freedom is left and we get the *physical effect* of the wave which has two degrees of freedom. We note that in TT gauge the metric perturbation is perpendicular to the wave-vector and the solutions to the wave equations take on a simple form:

$$h_{\mu\nu} = \exp^{ik^\mu x_\mu} \begin{bmatrix} 0 & 0 & 0 & 0 \\ 0 & h_+ & h_\times & 0 \\ 0 & h_\times & -h_+ & 0 \\ 0 & 0 & 0 & 0 \end{bmatrix}, \tag{1.15}$$

h_+ and $h_\times$ refers to the two different independent amplitudes that correspond to the two degrees of freedom remaining in the system. The frequency ω is dictated by the source model. If a coordinate system is affixed to the wave-frame and

the phase information is neglected, we arrive at the form,

$$h_{\mu\nu} = \exp^{kz-\omega t} \begin{bmatrix} 0 & 0 & 0 & 0 \\ 0 & h_+ & h_\times & 0 \\ 0 & h_\times & -h_+ & 0 \\ 0 & 0 & 0 & 0 \end{bmatrix}_{XY} \tag{1.16}$$

The components of the wave are separated into an orthogonal polarization basis called plus and cross respectively. Both components are transverse to the propagation of the wave, which reduces the dot product in the exponential to the value of $\overrightarrow{k}$ along the propagation direction (here denoted by z). The X and Y subscripts refer to the projection of the polarizations onto an arbitrary plane defined as orthogonal to the wave propagation.

It is worth mentioning that even though the gravitational wave equation is very similar to the equation of wave in electromagnetism, in electromagnetism, the wave equation is exact whereas the general relativistic wave equations are the solutions to the approximate linearized field equations.

The dynamics of the merger of two compact objects will be discussed in details later in this work. However, some of the most important features of the systems emitting gravitational wave are noted here. Such as the rate of the loss of energy through emitting GW and the time duration of the collapse of the two objects into each other.

In principle, one could estimate the luminosity of a merger. To make an estimation on the time it takes for a binary to collapse, one could use the simple fact that the loss of energy through the emission of the gravitational wave is provided by the change in binding energy of the binary [2]:

$$E = -\nu M v^2/2 \tag{1.17}$$

$$\dot{E} = -\mathcal{L} \tag{1.18}$$

Using the following formula for the angular frequency:

$$\dot{\omega} = \frac{\dot{E}}{dE/d\omega} = \frac{96}{5c^5}(G\mathcal{M})^{5/3}\omega^{11/3} \tag{1.19}$$

Where $\mathcal{M}$ is the chirp mass defined by $\nu^{3/5}M$. ν is the symmetric mass ratio defined by $\nu = \mu/M$ and $\mu = m_1 m_2/M$ and M is the total mass. For the equal mass binaries, ν is equal to $1/4$. The importance of this parameter, Chirp mass, will be discussed later. Eventually, the time that takes for the binary to merge can be estimated by the following (merging binary corresponds to angular frequency of infinity, and the time it takes for the binary to merge is calculated from a certain initial angular frequency): [2]

$$\tau = \frac{5c^5\omega_0^{-8/3}}{256(G\mathcal{M})^{5/3}} = 1000s \left(\frac{1.22M_\odot}{\mathcal{M}}\right)^{5/3} \left(\frac{10Hz}{f_0}\right)^{8/3} \tag{1.20}$$

Where f_0 is the frequency of the gravitational wave. One can calculate this time for different binaries, here comes some examples: For a binary with equal

masses of $M_\odot$ and orbital frequency of 0.0001 Hz, it takes 85 million years to merge. For a binary consisting of two neutron stars of equal masses $1.4M_\odot$ and orbital frequency of $3.58*10^{-5}$ it takes 300 million years to merge. As the binary shrinks, the compact objects get closer to each other. At some point they begin to rotate faster and faster, then after a while the orbit becomes unstable and the two objects dive into one another causing a huge explosion. The frequency at which the objects change their behaviour is around 440 Hz.

1.1 Gravitational Waves detectors

As we know in the theory of general relativity, a freely falling object alone can not realize whether it's in a gravitational field or not, only the deviation of two geodesics of test masses can reveal this information. Therefore, detecting GW is possible through measuring its effect on relative displacements of test masses. Instruments built to detect such waves are interferometers. Interferometers in general are used widely in science. The similarity among all of them regardless of their purpose is that they function by merging two or more sources of light. A very common type of interferometer is Michelson interferometer which was first built in the 1880s by Albert Abraham Michelson. These type of interferometers is adopted in gravitational wave detection. To understand how they function, imagine the following experiment on infinitesimal test masses (so that their gravitational interactions are negligible): Imagine three test masses on a plane such that they form a L shape figure and the direction normal to the plane is along the incident GW. Let's call the later direction along the z axis and the two test masses along the x and y axes. Also consider them as freely falling objects, so that they don't experience any other forces than gravitational force. If the incident GW has only h_+ polarization, it will cause an equal change in the distances between the mass on the x axis and the middle and between the mass on the y axis and the middle, such that the increase of one happens simultaneously with the decrease of the other and then it turns role as the polarity of the wave changes. On the other hand, if the incident GW had $h_\times$ polarization, there would not be any changes among the test masses on x and y direction, therefore in our set-up there wouldn't be any effect up to first order but if the system was turned by 45°, the same pattern as the one discussed earlier would happen. It's worth mentioning that the change in the separation of two test masses are similar with another pair of test masses as long as they are placed in the same direction; i.e the same fraction of the initial separation changes for all the pairs in the same direction. This property which is referred to as "tidal" is used in constructing interferometers. Now imagine the vertex mass is equipped with a lamp that produces small pulses of light and the two end masses have mirrors who reflect the pulses back to the vertex simultaneously. In the absence of GW, the lengths of the so called arms can be measured by the time that it takes for the flashes of light to arrive back to the vertex. As the incident GW arrives, these initial separations get disturbed and as a result the time that it takes for the pulses to reach the vertex differs. Take the incident

GW as following:

$$h^{\mu\nu} = h(t)\hat{h_+} \tag{1.21}$$

The time needed for the light to travel from the vertex to the mirror fitted on one of the end masses and to be reflected back to the vertex can be calculated by the following integrals. First, the interval between the two space-time events is:

$$ds^2 = g_{\mu\nu}dx^\mu dx^\nu = (\eta_{\mu\nu} + h_{\mu\nu})dx^\mu dx^\nu = -c^2dt^2 + (1 + h_{11}(2\pi ft - kz))dx^2 = 0 \tag{1.22}$$

Then the time for the light beam to travel from the vertex to the mirror is:

$$\int_0^{\tau_{out}} dt = \frac{1}{c}\int_0^L \sqrt{1 + h_{11}(2\pi ft - kz)}dx \approx \frac{1}{c}\int_0^L \left(1 + \frac{1}{2}h_{11}(2\pi ft - kz)\right)dx \tag{1.23}$$

Where the square root got simplified using a binomial expansion because $h \ll 1$. The time for the flash light to come back to the vertex is:

$$\int_{\tau_{out}}^{\tau_{rt}} dt = -\frac{1}{c}\int_L^0 \left(1 + \frac{1}{2}h_{11}(2\pi ft - kz)\right)dx \tag{1.24}$$

The total time is the sum of these two integrals.

$$\tau_{rt} = \frac{2L}{c} + \frac{1}{2c}\int_0^L h_{11}(2\pi ft - kz)dx - \frac{1}{2c}\int_L^0 h_{11}(2\pi ft - kz)dx \tag{1.25}$$

One could replace t by $\frac{x}{c}$ for the first part and by $\frac{2L-x}{c}$ for the second integral. However, considering $2\pi f_{gr}\tau_r t \ll 1$, it's then possible to treat the metric perturbation constant during this travel time. The same equation for time is valid for the other arm of the instrument, only that instead of h_{11} there will be h_{22} involved, as the other arm is in the y direction. Given the fact that the time difference between the arriving pulses from the two ends without any incident GW is $\frac{2L}{c} - \frac{2L}{c} = 0$, in the presence of GW this changes into:

$$\Delta\tau(t) = h(t)\frac{2L}{c} \tag{1.26}$$

One can express the travel time difference in terms of phase shift as one replaces the lamp with lasers:

$$\Delta\phi(t) = h(t)\tau_{rt0}\frac{2\pi c}{\lambda} \tag{1.27}$$

Where $\tau_{rt0} = \frac{2L}{c}$. This equation emphasises that the longer the arm of the interferometer is, the bigger the phase shift gets, therefore interferometers with very large arms have better sensitivities. [3]

Laser Interferometer Gravitational Wave Observatory (LIGO) in the US consists of two large observatories with a mirror placed in four kilometers away from them. This is the most obvious difference between typical Michelson interferometer and Gravitational wave detector: the scale. The one Michelson and Morley constructed to use for their famous experiment of studying "aether" was about 1.3m long. The longer the arm is, the better the sensitivity becomes. LIGO can detect displacements at the order of ten thousandth of the size of a proton. For this precision, even a four Kilometers long arms does not suffies. Therefore, the other difference between a typical interferometer and LIGO plays a role: the Fabry-Perot cavities. Extra mirrors that are placed in each arm near the beam splitter to make the light beam bounce back and forth up to three hundred times before being merged into the other beam from the other arm. This way the effective traveled distance for the light beam becomes twelve thousand Kilometers instead of four Kilometers. LIGO had made three runs up to now. The first run made the first three detection of GW emitted from black hole mergers. In the second run, eight detections were made, where seven of them was from black hole mergers and one from the very first neutron star merger detected. The last run made the detection of a merger of a neutron star and a black hole. LIGO made ninety detections in total from 2008 till this day. There is another ground based interferometer called Virgo placed near the city of Pisa, Italy. The arms are three kilometers long. Virgo is a Michelson interferometer, the mirrors are suspended and its laser operates in vacuum for it to be as isolated as possible from external disturbances. LIGO and Virgo were both later replaced by more sensitive detectors, which are referred to as advanced LIGO and Virgo. The other ground based GW observatory is KARGA located in Japan. It's again a Michelson interferometer, the arms are three kilometers and the instruments and the mirrors are suspended like Virgo but this detector is built under ground.

As discussed earlier, the displacement of the interferometer or the change in phase increases as the arms get longer. LIGO, Virgo and KARGA are all ground based detectors where the distances are limited. The figure below shows the Power Spectral density of LIGO, Virgo and KARGA.

The plot below [4] indicates the sensitivities of each interferometer at different observing runs.

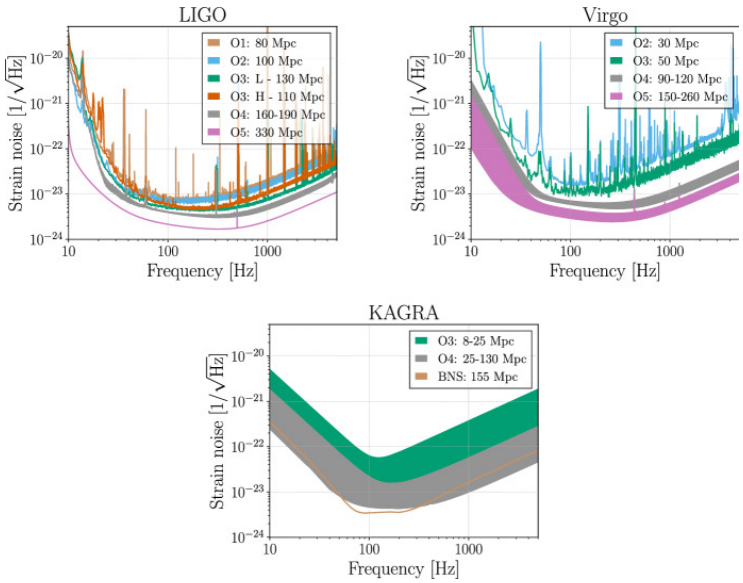

Figure 1.1: This figure is directly taken from [4]. aLIGO (top left), AdV (top right) and KAGRA (bottom) target strain sensitivities as a function of frequency. The quoted range is for a 1:4 $M_\odot$ P 1:4 $M_\odot$ BNS merger. The BNS range (in mega parsec) achieved in past observing runs and anticipated for future runs is shown. The O1 aLIGO curve is taken from the Hanford detector, the O2 aLIGO curve comes from Livingston. In each case these had the better performance for that observing run. The O3 curves for aLIGO and AdV reflect recent performance. For some runs the anticipated ranges are shown as bands reflecting the uncertainty in the impact of improvements and upgrades to the overall sensitivity. Detailed planning for the post-O3 to O4 period is now in progress and may result in changes to both target sensitivities for O4 and the start date for this run. The KAGRA BNS curve may be realized by detuning the signal recycling cavity to significantly improve the BNS range to 155 Mpc once design sensitivity is reached.

Laser Interferometer Space Antenna (LISA) on the other hand is the first space based observatory for GW detection made out of three space crafts making an equilateral triangle of side-length two and a half million Kilometers. Having long distances causes bigger change in time differences, therefore the interferometer gets more sensitive to weaker waves (smaller amplitudes), however, its sensitivity to high frequency waves decreases, because the wave length gets larger than the side length therefore the phase change detection of only one pulse would not be possible anymore. One important advantage of building interferometer in space is to get rid of all ground based noises that reduces the sensitivity of the observatory to small frequency GW.

Some sources to detect for LISA are the merger of massive black holes in the center of galaxies and extreme mass ratio inspirals.

Einstein Telescope is the future project based in Europe on new generation of ground based detectors aiming to detect GW and test general theory of gravity in strong field.

1.2 Recent results

There are in total three observing runs of events which refers to the coalescences of either two black holes (BBH), binary neutron stars (BNS) or a system of one black hole and one neutron star.

The first observing run (O1) of Advanced LIGO and Virgo detectors, from September 2015 to January 2016, resulted in observing three binary black hole mergers. The second run (O2), from November 2016 to August 2016, resulted in the first detection of a binary neutron star and seven binary black hole mergers. [5] The first gravitational wave transient catalog, GWTC-1, contains eleven events from these two observing runs. The third observing run was separated into two parts. GWTC-2 contains the first part of third run, and added thirty nine new events to GWTC-1. However, the same data from O3a were later re-analyzed, GWTC-2.1 and discovered eight new events compared to the first analysis, but it resulted in disapprovement of three event previously discovered in GWTC-2 as the astrophysical probability of them were found to be less than 50%. Therefore the total number of event till then was fifty five. Eventually, GWTC-3 brought thirty five new detection by analyzing the second part of third observing run, O3b, between November 2019 till March 2020. The total number of observed binaries are ninety until now. Figure bellow shows an interesting development of detected events in time-volume, which is the observing time multiplied by the Euclidean sensitivity volume of the detector network. A conventional way of measuring sensitivity is the average distance that a fixed BNS of $1.4M_{\odot} - 1.4M_{\odot}$ inspiral can be observed with a signal-to-noise ratio (SNR) of 8. [6] The rather fast increase in number of detection from O1, three events, and O2, eleven events, to O3, ninety events, can be explained by this figure. The number of detection is proportional to the BNS time-volume. Since the sensitivity of the detector improves, the BNS time-volume increases cubicaly as the increase in sensitivity causes an increase in detectable radius therefore the detectable volume increases cubicaly. Therefore the rate of discovering new events increases as the figure shows.

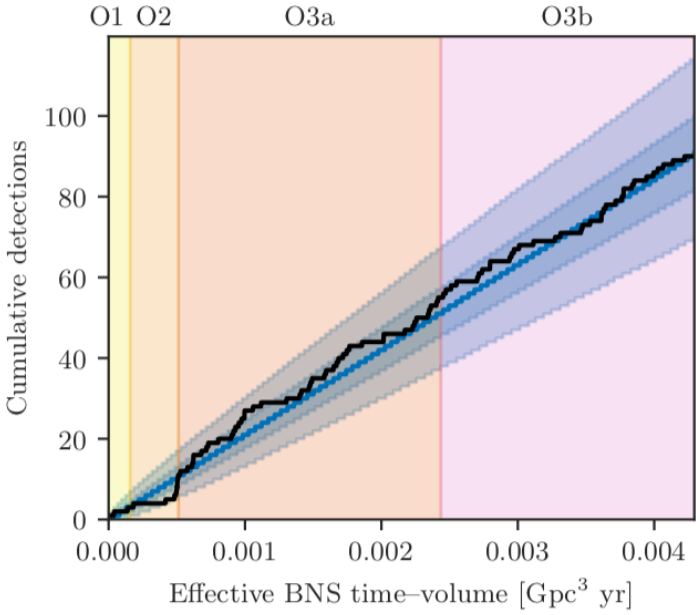

Figure 1.2: This figure is taken directly from [7]. The number of CBC detection candidates with a probability of astrophysical origin $p_{astro} > 0.5$ versus the detector network's effective surveyed time–volume for BNS coalescences [3]. The colored bands indicate the different observing runs. The final data sets for O1, O2, O3a and O3b consist of 49.4 days, 124.4 days, 149.8 days (177.2 days) and 125.5 days (142.0 days) with at least two detectors (one detector) observing, respectively. The cumulative number of probable candidates is indicated by the solid black line, while the blue line, dark blue band and light blue band are the median, 50% confidence interval and 90% confidence interval for a Poisson distribution fit to the number of candidates at the end of O3b.

The x-axis shows the volume that have been surveyed in one year. It's interesting to note that even though the detecting time of O2 and O3b were almost the same, the time-volume is so different because the sensitivity of the detector has increased.

The figure bellow 1.3, from the third catalog of gravitational wave detection, illustrates the sheer number and our growing population of detected events.

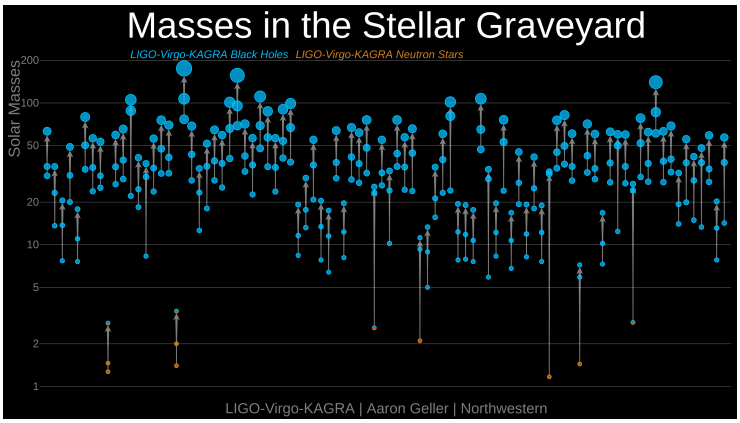

Figure 1.3: Compact object masses. Each circle represents a different compact object and the vertical scale indicates the mass as a multiple of the mass of our Sun. Blue circles represent black holes and orange circles represent neutron stars. Half-blue / half-orange mixed circles are compact objects whose classification is uncertain. Each merger involves three compact objects: two merging objects and the final resulting object. The arrows indicate which compact object merged and the remnant they produced. Credits: LIGO Virgo Collaboration/Frank Elavsky, Aaron Geller/Northwestern.

Compact objects of less than $3M_\odot$ are most probably considered as neutron stars. The internal structure of neutron stars are yet not completely known, but one tend to claim that super fluidity of neutrons in the core must be true. Out of all 35 new detected events in the third catalog, 32 are binary black hole coalescences and the remaining three are most probably black hole-neutron star coalescences and no binary neutron star was detected. The three possible neutron star-black hole coalesences are GW191219-163120, GW200115-042309 and GW200210-092254. The characteristic of the first coalescence is that the masses are highly unequal, with black hole being almost 26 times more than the neutron star. (Black hole of 31 $M_\odot$ and neutron star of $1.2M_\odot$ which made the least massive neutron star ever observed.) The mass ratio in the second coalescence is 4.28 (Black hole of 6 $M_\odot$ and neutron star of $1.4M_\odot$). The third observed coalescence is slightly less sure. The mass ratio is 8.57 (Black hole of 24 $M_\odot$ and neutron star of 2.8 $M_\odot$), however, the lighter object could indicate either a light black hole or a heavy neutron star.

1.3 Non-linear memory

The effect of memory can be best detected by the relative displacement of two freely falling masses accused to the passage of gravitational wave. This can rise from a linear memory or non-linear memory. Unbound masses with non oscillatory motion can produce linear memory, like hyperbolic orbit or two-body scattering. However, non-linear memory is due to the gravitational waves coming from gravitational waves themselves. Any source of gravitational wave produces non-linear memory which can be deducted from the difference of the

gravitational wave amplitude at early times and at late times:

$$\Delta h_{+,\times} = \lim_{t\to\infty} h_{+,\times} - \lim_{t\to-\infty} h_{+,\times}. \tag{1.28}$$

This effect is a prediction of general relativity. Christodoulou memory is a kind of non-linear memory. Bound gravitational systems produce this type of memory since the gravitational wave is oscillatory in these systems. It arises from the gravitational-wave stress–energy tensor's contribution to the distant gravitational-wave field. [8] It is the non-oscillatory contribution to the gravitational wave amplitude. Travelling GWs themselves can be considered as sources of gravitational radiation. The footprint that a GW leaves after passing through a point can be detected by GW detectors, however, this effect is so small that makes it challenging. To be more precise on this matter, it is worth mentioning that one can realize that the gravitational field is non-linear by looking at Einstein's equation:

$$R^{\mu\nu} - \frac{1}{2} g^{\mu\nu} R = 8\pi T^{\mu\nu}, \tag{1.29}$$

Where $T^{\mu\nu}$, $R^{\mu\nu}$ and $g^{\mu\nu}$, are stress energy tensor, Ricci tensor and metric respectively. (Note that in this equation, we set $G = c = 1$.) One can claim that the non-linearity of the memory is originated by that.

Non-linear memory is the gravitational wave generated from the gravitational wave itself. It is an additional component that is produced by gravitational waves and is directly coming from the field equations, e.g. they are generated by the contribution of gravitational waves itself.

Figure 1.4 shows the h_+ polarization of waveform generated by the SXS gravitational wave data base for a merger of a non-spinning binary compact object of equal masses.

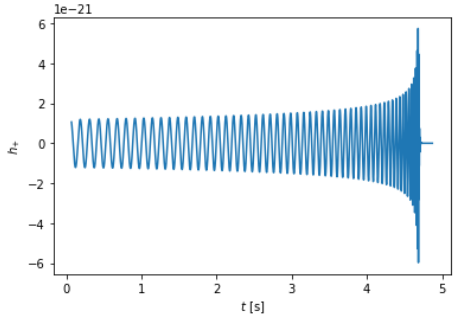

Figure 1.4: h_+ polarization of the waveform 0001: $\ell = 2$ system is at distance of 100 Mpc and the total mass is 100 $M_\odot$.

Figure 1.5, shows the memory term contribution to the waveform 0001 represented in figure 1.4:

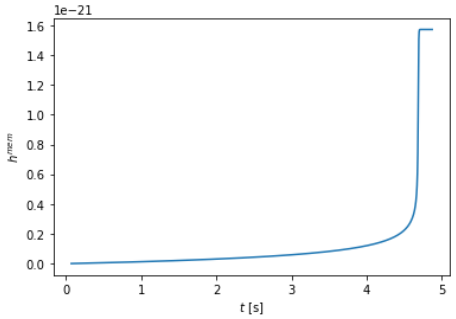

Figure 1.5: Memory term contribution of the waveform 0001: $\ell = 2$ and $|m| = 2$

The shift in the plot shows the displacement of the waveform. In order to see this effect on the whole waveform, here is a plot showing both memory and wave form without memory summed up:

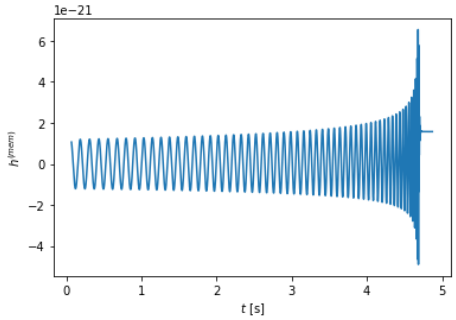

Figure 1.6: Waveform: 0001, the total waveform mode $\ell = 2$ and $|m| = 2$

Chapter 2

Properties of gravitational waves emitted from binary black holes

2.1 Evolution of binary black hole system

In this section we outline how binary black holes evolve under the presence of self gravity. As they are assumed to be in vacuum, the only way for them to evolve is through interacting with themselves. They loose energy and angular momentum by radiating gravitational waves. The gravitational waves' frequency emitted from a binary is mainly (under the assumption of quasi-circular orbit) twice as the frequency of the orbit. As gravitational waves carry energy and momentum away from the sources this causes them to inspiral towards each other. The orbit gets smaller, the frequency of the orbit increases and the system gets more relativistic eventually merging. If the binary is eccentric, the eccentricity becomes more circular (quasi-circular). However, if they have spins aligned to the angular momentum, the evolution of the orbit stays in the plane. But if the spin is misaligned to the angular momentum the orbit precesses. Thus the system undergoes three stages, first the shrink of their orbit, inspiral stage, then the transition from inspiral to the plunge/merger stage leading to formation of single remnant black hole, then the remnant oscillates which is called the ringdown stage. The process of transition from inspiral to the coalescence can go on up to millions of years. The coalescence is a catastrophic event, emitting extremely luminous gravitational radiation.

The modelling of gravitational waves from the compact binary coalescence is a challenging task as there exists no accurate analytical solution to the two-body problem in general relativity. Several techniques are hence developed to solve approximately and numerically the evolution equation. Numerically one can solve Einstein's equation accurately but the computational cost of doing

so can be prohibitive especially if one needs to have a long time evolution. This method is known as Numerical Relativity (NR). Analytically one can solve the Einstein's equation approximately by using perturbative methods, these methods often require a physical parameter which is small so one can expand the solution around that parameter. Post-Newtonian theory is a prime example of such an approximate solution where the system is evolved around v/c where v is the velocity of the objects and c being the speed of light. Binary black hole systems towards the end of the inspiral part can reach velocities closer to that of speed of light so post-Newtonian theory can not be used for the full signal. Another method which solves Einstein's equation in a perturbative way is called the "self-force". The small parameter is the mass ratio of the companions in self-force method. We also have an analytical solution which maps the two-body problem to an effective one body problem making the system solvable accurately, this method is called Effective one body (EOB) approach.

Lots of research has been done on modeling the sources of gravitational waves and plenty of effort has been dedicated to detecting and analyzing the data. NR simulations are used to predict waveforms of the merger states of two compact objects like black holes, as this stage is the highly relativistic regime. NR however as mentioned earlier is restricted by computational cost which makes the generation of NR simulations possible and useful only when the system is highly relativistic and also having smaller mass ratio (since high mass ratio require a much longer in time simulation). Post-Newtonian approach is used for a wide range of mass ratios however does not apply well for the highly relativistic areas and hence is used only for the early inspiral part of the signal. The perturbation method is useful only when the mass-ratio is high, around 10^3. This is described in figure 2.1.

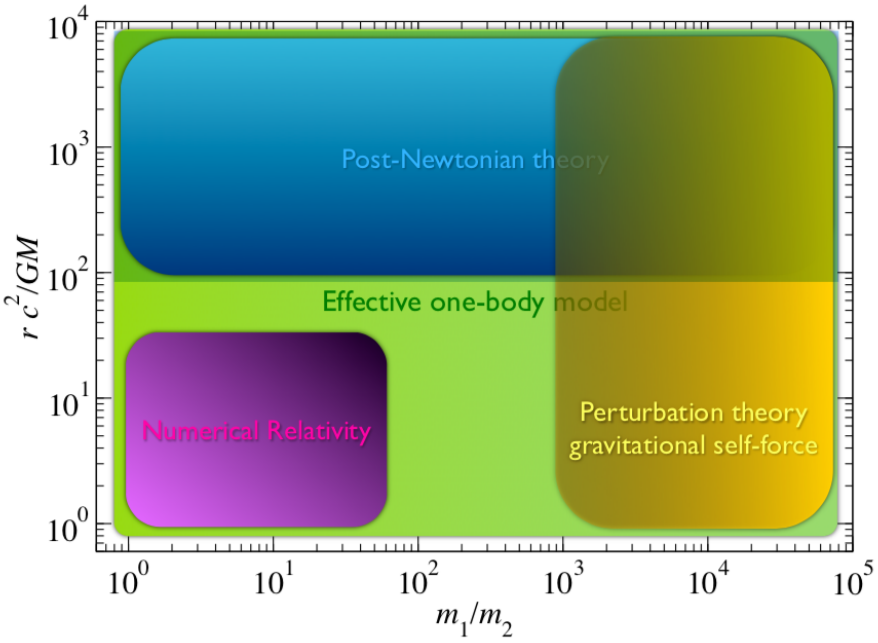

Figure 2.1: This figure is taken directly from [2]. Here the y-axis represents the separation of orbits which in turn is related to the velocity of the objects. One can clearly see that post-Newtonian formalism is valid only when the orbits are well separated. The x-axis corresponds to the mass ratio of the system for high mass ratio the perturbation theory (self-force) formalism is valid. Effective one body formalism covers the full parameter space.

2.1.1 Post-Newtonian formalism

Post Newtonian method is used for the case of having a slowly moving and weekly stressed and weekly gravitating source. As mentioned earlier, this formalism basically expands the waveforms in the powers of v/c. Writing the linearized equation and having the harmonic gauge condition in mind, $\partial_j h^{ij} = 0$, one gets to the following equation:

$$\begin{aligned} \Box h^{ij} = \frac{16\pi G}{c^4}|g|T^{ij} + \Lambda^{ij} = \frac{16\pi G}{c^4}\tau^{ij}\Box h + h_{,i,j} - h^k_{i,k,j} - h^k_{j,k,i} \\ = -16\pi(T_{ij} - \frac{1}{2}T\eta_{ij}) \end{aligned} \tag{2.1}$$

Where T^{ij} is the stress energy tensor.

Under the boundary condition of no in-coming gravitational radiation one may solve this equation by using retarded greens function as follows:

$$h^{ij}(t,\mathbf{r}) = -\frac{4G}{c^4}\int \frac{\tau^{ij}(t - |\mathbf{r}-\mathbf{r}'|/c, \mathbf{r}')}{|\mathbf{r}-\mathbf{r}'|}d^3r' \tag{2.2}$$

Which can be simplified to the following by assuming the distance is much bigger than the size of the source:

$$h^{ij}(t,\mathbf{r}) = -\frac{4G}{c^4}\int T^{ij}(t - r/c + \mathbf{n}.\mathbf{r}'/c, \mathbf{r}')d^3r' \tag{2.3}$$

As the source is slowly moving, one can use a small parameter v/c for the following ratio:

$$|T^{0i}/T^{00}| \sim \sqrt{|T^{ij}/T^{00}|} \sim \sqrt{U/c^2} \ll 1 \tag{2.4}$$

Where U is the Newtonian potential energy of the source. The gravitational field at linear order in G can be derived by expanding the integral 2.3 in powers of v/c:

$$h_{ij}^{TT} = \frac{2G}{c^4 R}\Sigma_{kl}\mathcal{P}_{ijkl}(\mathcal{N})\left[\frac{d^2}{dT^2}Q_{kl}(T - \frac{R}{C})\right] \tag{2.5}$$

Where $R = \sqrt{\Sigma_i X_i^2}$ is the distance to the source, N is the unit vector from the source to the observer, $\mathbf{X}/R$ and $\mathcal{P}_{ijkl}$ is the TT projection operator. $\mathcal{P}_{ij} = \delta_{ij} - N_i N_j$. Q_{ij} is the following:

$$Q_{ji}(t) = \int_{source} d^3\mathbf{x}'\rho(t,\mathbf{x}')\left(x_i' x_j' - \frac{1}{2}\delta_{ij}x'^2\right) \tag{2.6}$$

Where ρ is Newtonian mass density.

There are several methods to approach the two body problem as long as the sources are moving slowly and masses are comparable and we are in the weak field and not relativistic. These methods are the post Newtonian and post Minkowskian, the canonical Hamiltonian formalism and the effective field theory. It is important that we get the same results out of all different methods and that they agree with each other. These approaches work well for two body systems with mentioned features until before approaching the last stages of the inspiral as it gets more sensitive for higher order post Newtonian approximation. The figures below compares waveforms generated by two different methods, Post Newtonian (PN) and Effective one body (EOB). EOB is explained later in this chapter.

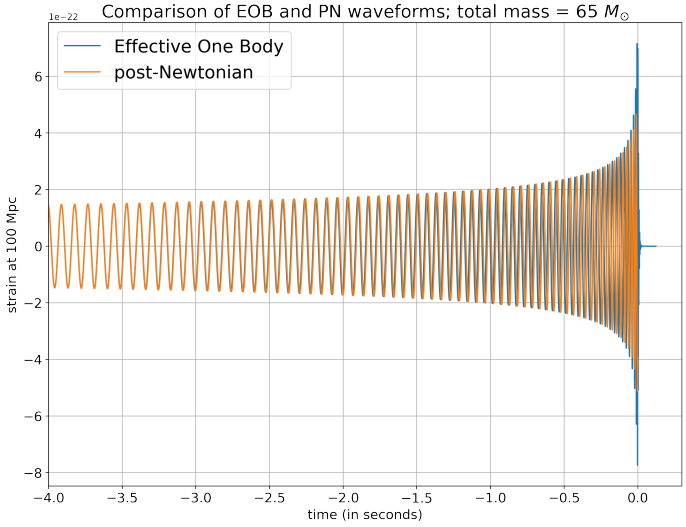

(a) Full Waveform

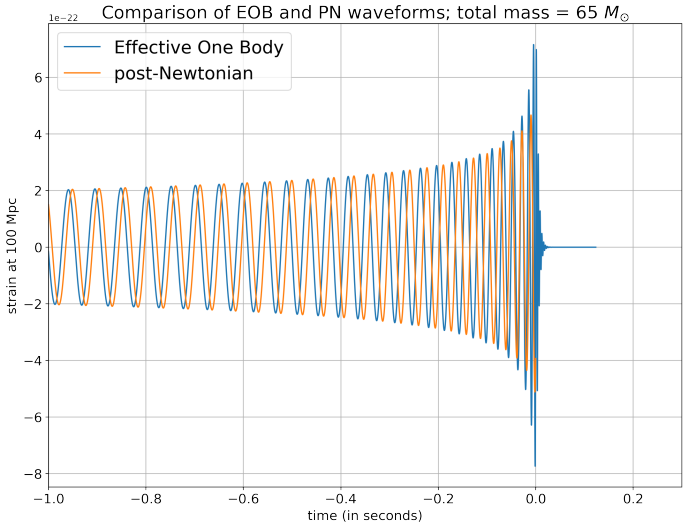

(b) Zoomed in near the merger

Figure 2.2: We plot the post-Newtonian waveform (in orange) with the effective one body waveform (EOB) together for the same parameters of mass ratio and total mass. We can see that earlier in the evolution when the orbits are well separated PN matches very well with the EOB waveform. but as the system get closer the PN waveform does not have the same phase as the EOB waveform. Also only the EOB waveform is generated when the black holes plunge and ringdown

2.1.2 Perturbation theory gravitational self force

For the case of different mass ratios and heavy masses the orbits are expected to be highly eccentric and relativistic. To solve the two body problem and calculate the wave forms one may expand the field equations in the mass ratio defined

by $q = m/M$, m being the smaller mass and M the bigger. The perturbation of the metric from the background metric can be expanded in powers of mass ratio as follows:

$$h_{ij} = \Sigma_n h_{ij}^{(n)} \tag{2.7}$$

Note that in spite of post Newtonian formalism, h_{ij} is the deviation of the metric from the background metric and not the deviation of the background metric from Minkowskian metric. For the case of very small q, the test mass rotates around the heavy mass in a quasi circular orbits. The perturbation caused by the test mass creates a field that acts back on the motion of the test mass itself (radiation-reaction force) and changes the orbit ever farther that circular motion. This is a dissipative field that contributes to the motion of the test mass in a frictional way. Although this effect if of the order of q^2, after a large amount of cycles the overall effect is non negligible.

2.1.3 Numerical relativity

Numerical relativity is probably the only method to solve the dynamics of compact binary system in a fully non-linear regime. The two body problem in GR is much more complex than in Newtonian since space and time are couples in a complex manner in Einstein's equations, which is responsible for the non-linearity nature of it. Another complication that occurs in comparison with Newtonian two body problem is due to the dissipation of energy of the binary system because of gravitational interaction. Eventually, instead of one ordinary differential equation in Newtonian regime, we have a system of coupled partial differential equations (PDEs). This forms an initial boundary value problem (IBVP). To numerically solve them, one needs to specify boundary conditions in a way that they are physically correct and satisfy the constraints like the Einstein constraint equation [9]. The outer boundary is that there is no in going GW from infinity. Equations should be formulated in a way that shows the space-time solution continuously depends on the initial condition, accordingly, a computational algorithm needs to be implemented which results in a time evolution that continuously depends on initial data. A natural way to start building the initial data is to modify the current analytical solutions of BH, for instance, the Schwarzschild solution. Also, the gauge condition must be chosen numerically suitable. Since some of the evolution parameters are not specified by Einstein equations, one needs to chose them in a way that their choice keeps the physical properties of the space-time invariant. Another important step is discretization. Computers work with finite arrays of integer numbers or binary numbers. Therefore, in the process of calculating differential equations with them, defining a function is already challenging, also their derivatives. There exists a few methods to do this process, which is called "discretization". Some that have been applied to NR simulations of BBH are "finite differencing" and "spectral methods". [9]

2.1.4 Effective one body formalism

Effective one body formalism known as EOB is an analytical approach that is made by combining perturbation theory and PN expansion. This approach was meant to model analytically the motion and the radiation of a binary system through all stages of its evolution. EOB was confirmed by NR simulations for several different situations such as the adiabatic transition from the inspiral to merger, the short merger phase, estimations of the radiated energy at the end of inspiral, merger and ringdown. [2] After these confirmations, EOB was extensively used for leading-order spin effects and higher order PN terms. Therefore, EOB is able to predict the full wave form of coalescing binary.

There are a few points that EOB adopts like the Hamiltonian (conservative two body dynamic), the radiation reaction force and the GW emitted. In order to construct these concepts in EOB, first, the assumption that the system of comparable mass is a deformation of test particle limit has been taken into account, and second, got inspired by the previously derived results. For instance, the EOB merger ring down wave form was implanted by the results in the close limit approximation. In this approximation one changes from two body problem to one body description which is close to the peak of the BH potential barrier. One could claim that the idea of EOB is to replace the physical real conservative dynamics of a system, such as spins and masses, by an auxiliary and effective parameters defined as followed: a mass $\mu = m_1 m_2/(m_1 + m_2)$ moving with and effective spin $\mathcal{S}_*(\mathbf{S}_1, \mathbf{S}_2)$ in a deformed Kerr-liked geometry $g^{eff}_{\mu\nu}(\mathcal{M}, \mathcal{S}_{Kerr}; \nu)$ with mass $\mathcal{M} = m_1 + m_2$ and spin $\mathcal{S}_{Kerr}(\mathbf{S}_1, \mathbf{S}_2)$. ν is the deformation parameter which is the same as the symmetric mass ratio, $\mu/\mathcal{M}$. ($\nu = 1/4$ for equal masses) It is worth mentioning that it becomes quite useful to think quantum mechanically in order to obtain such a mapping between real dynamics and effective dynamics. Meaning instead of considering the classical Hamiltonian's, one could consider the energy levels of quantum bounded states respective to the Hamiltonian operators.

2.1.5 Order of magnitude

To make an estimation on the brightness of the binary coalescence, one may have a look at the leading order expression of the gravitational wave luminosity. The equation comes in the source quadruple moment given by the following:

$$\mathcal{L} = \frac{G}{5c^5}[\frac{dQ^3_{ij}}{dT^3}\frac{dQ^3_{ji}}{dT^3}] \tag{2.8}$$

Which is known as the Einstein quadrupole formula. Q_{ij} is the source quadrupole moment mentioned earlier in eq. 2.6.

Using eq. 2.8, for a system of masses m_1 and m_2 with d as their separation distance on a circular orbit, one can estimate the mentioned luminosity using eq.(6.10) of [10]:

$$\mathcal{L} = (32c^5\nu^2/5G)(v/c)^{10} \tag{2.9}$$

Where $\nu = m_1 m_2 / M^2$, M being the sum of the two masses and v is the orbital velocity given by $\sqrt{GM/d}$. As one can see in eq. 2.9, the binary is the most luminous if the orbital velocity is higher, relativistic, and if the mass ratio is smaller (thus ν is bigger). Most of the rotating objects in the universe do not have comparable masses and are nowhere close to being relativistic. The more compact they are, the stronger gravitating systems they become, which leads then to a higher orbital speed. Black holes and neutron stars are the most compact objects in the universe and indeed their system can become relativistic. As black hole binaries merge, their speed are at the order of $v/c \approx 1/\sqrt{2}$ [299.of 5]. The luminosity of this system is at the order of $10^{24}\mathcal{L}_{\odot}$. This brightness is somehow confirms the claim that binary systems of black holes and neutron stars (compact objects) are the best candidates to be detected and they are the main sources of gravitational waves for observations.

2.2 Examples of BBH evolutions

The development of the binary depends on some parameters such as the mass ratio, aligned spin and mis-aligned spin which are studied in the rest of this chapter. The goal is to learn how the wave form evolves differently if the system has different mass ratio or spin. Later on, in section four, we'll study the degeneracy of these parameters where we go through more detail.

2.2.1 Effect of mass ratio

Thanks to the SXS data base, one can plot the wave-form of numerous different BBH systems. Here, to see the effect of mass ratio on the evolution of the wave-form, five different systems are chosen who has no spin, same total mass but different mass ratio. All other parameters are kept similar among these systems.

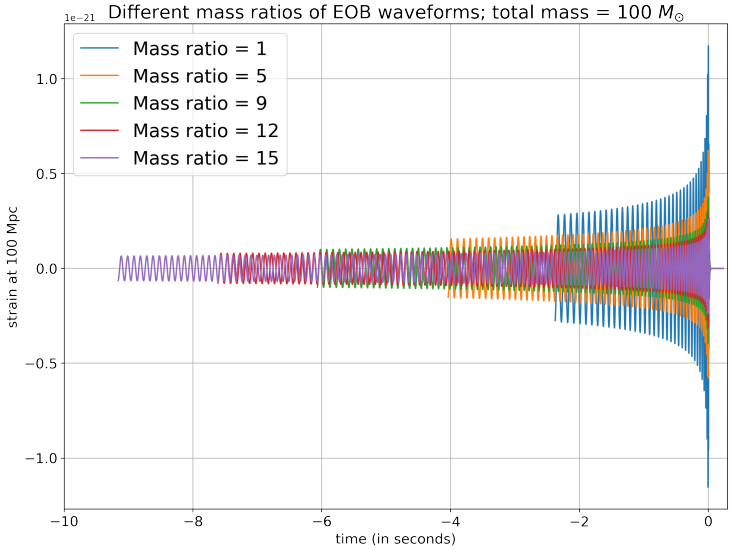

Figure 2.3: Comparison of the waveforms with different mass ratios. We plot effective one body (EOB) waveforms for the same parameters of total mass and distance and inclination angle but different mass ratios. Low frequency cut is 10Hz. We can see that the more similar the mass values are, the higher the amplitude gets.

Apart from the decrease of the amplitude by increasing the mass ratio, one can notice another response of the waveforms to the mass ratio: The time it takes for the system to merge increases. This fact can be inferred from the plot. A fix frequency is given to the waveform function as starting point. It can be seen in the plot that more oscillations are needed for a system with higher mass ratio to reach the coalescence, therefore it's longer expanded in time.

As it was almost predictable from the figure 2.3, the frequency of the waveform increases as the mass ratio gets bigger. Physically, one can conclude that systems made of masses of the same order loose energy easier (faster) than systems made out of a small mass and a big mass; as they need more oscillations to loose energy and get closer and eventualy collapse into each other.

2.2.2 Effect of aligned spin

Binary black holes with equal masses might have another parameter effecting their evolution, their spins. Spin of a binary can be either aligned or miss-aligned.

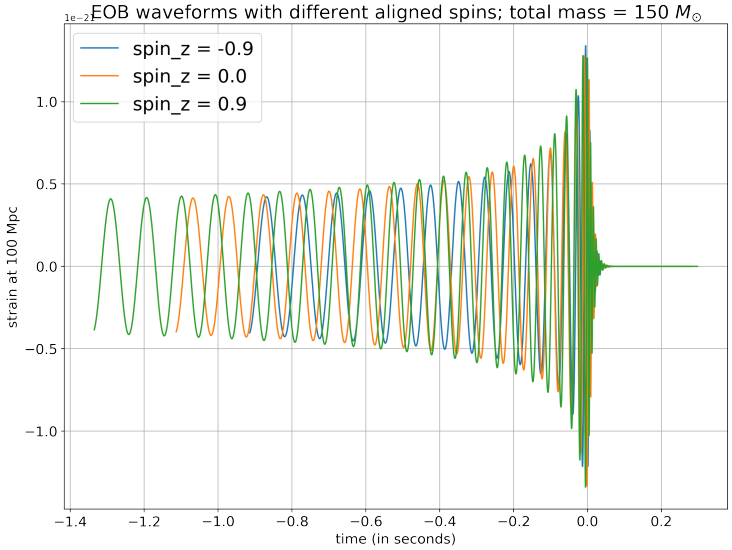

Figure 2.4: Comparison of the waveforms with different spins. We plot effective one body (EOB) waveforms for the same parameters of total mass, mass ratio, distance and inclination angle but different spins. We can see that the bigger the spin is, the longer the system needs to collide as the waveform with spin-z 0.9 (green) starts earlier than the one with spin-z 0.0 (orange) and the last one to start is the waveform with spin-z -0.9 (blue).

The figure above demonstrates the effect of spin on waveforms. One can conclude that the amplitude of the waveform is almost un-changed, however, a similar effect as the last section for different mass ratios occurs here. All three waveforms start from a fix frequency. The one with the highest aligned spin needs longer to reach the coalescence. Note that to solely have the effect of spin, the mass ratio of all three WFs are equal to one. It is worth mentioning that mass ratio is totally degenerate with aligned spin, and it has the same effect on frequency, but the effect is different regarding the amplitude.

To compare their frequencies, we transform the WF to Fourier space. The dominant frequency of the Fourier spectrum of the waveform SXS:BBH:0219 with effective spin of 0.2 is 9.58 Hz, the dominant frequency of the Fourier spectrum of the wave form SXS:BBH:0394 with effective spin 0.5 is 10.99 Hz and the dominant frequency of the WF SXS:BBH:0176 with effective spin 0.96 is 11.15 Hz.

2.2.3 Effect of misaligned spin (Precession)

System of binary masses are called non-precessing if either the two masses do not spin at all or their spin is aligned with the orbital angular momentum. In the following we represent the effect of misaligned spin on the waveforms.

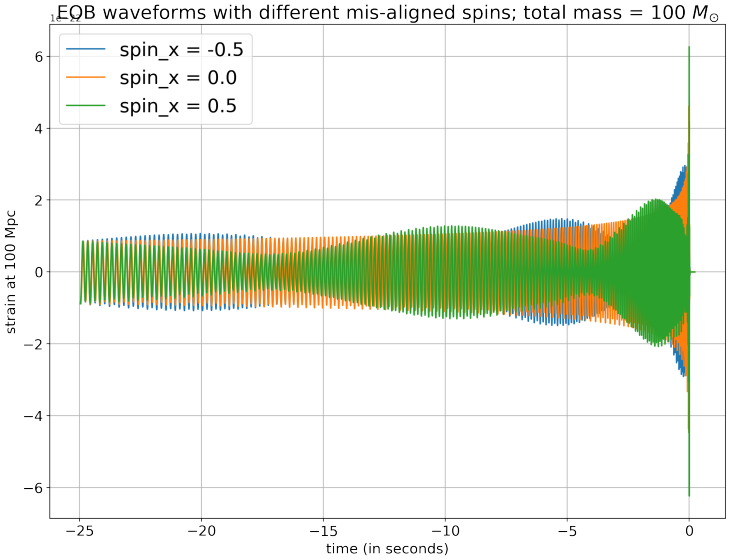

Figure 2.5: Comparison of the waveforms with different misaligned spins in x-direction. We plot effective one body (EOB) waveforms for the same parameters of total mass, mass ratio, distance and inclination angle but different misaligned spins, spin-x.

There are a couple of features one can notice. For instance, the green waveform looks the same as the blue one. So the sign of the spin does not make a change in the waveform (unlike the aligned spin). To see this better, the following plot only includes wave forms with +0.5 $spin_x$ and -0.5 $spin_x$.

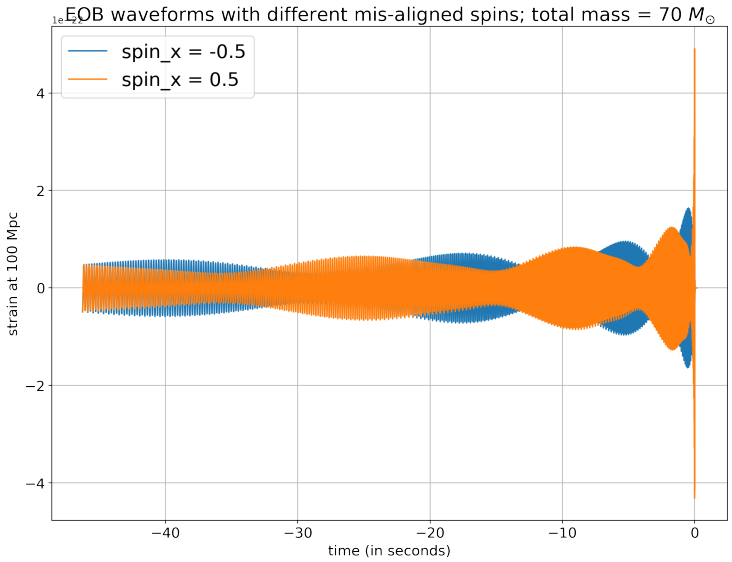

Figure 2.6: Comparison of the waveforms with different mis-aligned spins in x-direction. The total mass is decreased compared to the previous plot to get a denser waveform to easier compare them.

Another effect of mis-aligned spin in comparison to aligned spin is that the wave form is longer for non-precessing systems. Also, we have checked that the inclination angle does not effect anything.

We noticed a change in the wave forms as we plot the spin-y, which is slightly out of expectation as one might think that it's a matter of definition:

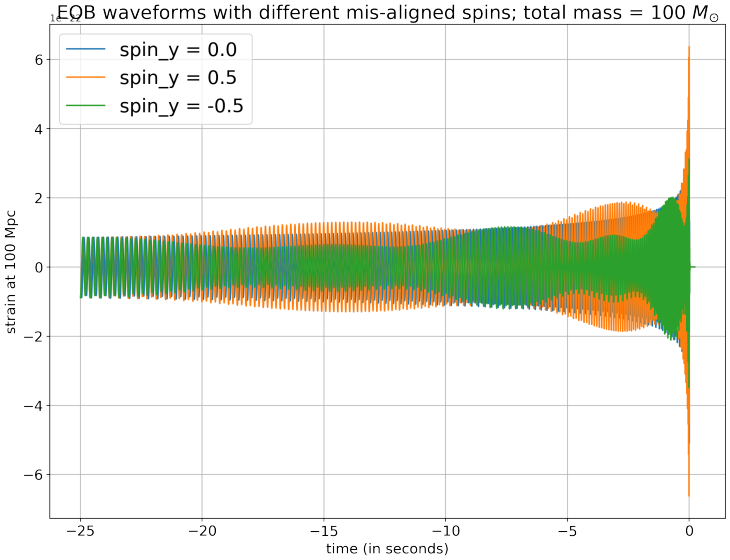

Figure 2.7: Comparison of the waveforms with different mis-aligned spins in y-direction. We plot effective one body (EOB) waveforms for the same parameters of total mass, mass ratio, distance and inclination angle but different misaligned spins, spiny.

The modulation of amplitude is the noticeable effect, the change in the amplitude for positive and negative mis-aligned spin.

Chapter 3

Non-linear memory

Introduction The passage of gravitational wave has a persistent effect on the space time region that the wave passed through. This physical effect is detectable by placing a detector in the path of the gravitational wave and is called memory effect which can happen by the gravitational wave emitted by displacement of a compact object or by an oscillatory movement of a binary black holes. The first example causes a linear memory and the later one causes a non-linear memory. Memory is a needed term in Poincare's extend of conservation laws, Bondi-Metzner-Sachs (BMS) conservation laws [11]. One can calculate the Poincare charge differences by measuring the corresponding energy and momentum fluxes based on Poincare's conservation laws. Also there are ten Poincare charges. However, memory effect has a role in the extension of Poincare's conservation law, BMS: the difference between the BMS charge changes and the corresponding energy and momentum changes is the memory effect. There are in total three types of memory effect. Displacement memory, spin memory and CM memory. The displacement memory, the most prominent one, is the memory that can be inferred by the change of arm length of the GW detector. The reason of the time delay of objects rotating in opposite direction is the spin memory, similarly, the time delay acquired by particles moving on different paths is due to CM memory. In BBH mergers, as mentioned earlier, the displacement memory is the leading memory, after that the spin memory is the strongest and CM memory comes at last. [11]

To calculate the three different memories, one needs to use numerical relativity methods instead of post Newtonian approximations because the latter doesn't give an answer to the BBH merger, the strongest phase or binary evolution in terms of memory generating. The displacement memory is the change that a gravitational wave endures between early times and infinite future. This affects the geodesic of a freely falling object being nearby. But the following question comes to mind: What can generate displacement memory and if any of the astrophysical sources could generate this effect with strong enough amplitude to be detected by current detectors? As mentioned earlier, the change in supermomentum of a source causes this effect. In principle, any isolated source

that radiates effective energy asymmetrically in gravitational field, can generate displacement memory. [12]

Zel'dovich and Polnarev computed the displacement memory of the scattering of stars. They stayed in the context of linear gravity. [13] Turner claimed that neutrinos emitted by supernovae can produce this effect as well. [12]

In the following lines, we give more detail on spin memory effect. Spin memory effect is the change in the magnetic parity part of the time integral of the GW strain from early times to infinite future, which is due to the fluxes of the angular momentum. [12]

Non-linear memory arises from the oscillatory movement of masses. It produces a non oscillatory term in the gravitational wave amplitude. There are methods to calculate the memory waveforms from an oscillatory gravitational wave time series which comes later in this chapter. First step is to derive the memory. We start by expanding the gravitational wave into spin weighted spherical harmonics [8]. There are two moment tensors appearing in the solution of the linear vacuum-wave equation of GWs, which are called radiative mass and current multipole moment tensors, $\mathcal{U}_{i_1,i_2,..,i_l}$ and $\mathcal{V}_{i_1,i_2,..,i_l}$, which can be expanded in terms of spherical harmonic tensors [8]:

$$\sqrt{2}R(h_+ - ih_\times) = \sum_{l=2}^{+\infty} \sum_{m=-l}^{l} (U_{lm} - V_{lm})_{-2}Y^{lm}(\Theta, \Phi) \tag{3.1}$$

U and V being their coefficients and (R, Θ, Φ) are the coordinates pointing towards the observer from the source. The non-linear memory can be calculated by the integral of the gravitational flux [14]. The radiative moments are related to some source multipole moments through a post Newtonian wave-generation formalism. These source multipole moments are derivable by integrals over the stress-energy pseudo-tensor of the matter and the field of source. The algorithm is non-linear, iterative which gives the following weak-field expansion for the mass multipole:

$$U_{lm} = I_{lm}^{(l)} + GU_{lm}^{(tail)} + GU_{lm}^{(mem)} \tag{3.2}$$

The first term is the l_{th} derivative of the mass moment. The last term is the memory contribution which is as follows:

$$U_{lm}^{(mem)} = \frac{32\pi}{c^{2-l}} \sqrt{\frac{(l-2)!}{2(l+2)!}} \int_{-\infty}^{T_R} dt \int d\Omega \frac{dE_{gw}}{dtd\Omega}(\Omega) Y_{lm}^*(\Omega) \tag{3.3}$$

Where $\frac{dE_{gw}}{dtd\Omega}$ is the energy flux and T_R is the retarded time. [8] The leading order of energy flux at l=2 can be derived as following:

$$\frac{dE_{gw}}{dtd\Omega} = \frac{1}{32\pi} \Sigma_{m,m'} I_{2m}^{(3)} I_{2m'}^{(3)} Y^{2m} Y^{2m'} \tag{3.4}$$

Therefore the leading order contribution of the memory part for a coalescence can be calculated by using equation 3.4 and integrating over Ω:

$$U_{20}^{(mem)(1)} = \frac{1}{14}\sqrt{\frac{5}{3\pi}} I_{22}^{(3)} I_{2-2}^{(3)} \tag{3.5}$$

$$U_{40}^{(mem)(1)} = \frac{1}{2520}\sqrt{\frac{5}{\pi}} I_{22}^{(3)} I_{2-2}^{(3)} \tag{3.6}$$

Which are the first derivative of the mass moment contribution to the memory. $I_{2\pm1}$ is zero considering only in-plane orbits. U_{lm} vanishes for odd l's. For l's higher than or equal to 6, the contribution is on higher orders of post Newtonian expansion. Non-zero m's has oscillatory effects on 2.5 and higher order post Newtonian terms which we ignore. Also, We ignore the radiative current contribution since it does not have a non-linear effect. Simplifying equation 3.1 by using equation 3.5 and 3.6 one gets the following for the memory [8]:

$$h_{+}^{(mem)} = \frac{\eta M}{384\pi R} sin^2\Theta(17 + cos^2\Theta) h^{(mem)} \tag{3.7}$$

$$h^{(mem)} = \frac{1}{\eta M}\int_{-\infty}^{T_R} |I_{22}^{(3)}(t)|^2 dt \tag{3.8}$$

Where $h_{\times} = 0$ considering the standard choice of the polarization tensor and circularized orbits. The above equation is the memory of only dominant mode ($l = 2, m = |2|$), whereas Paul D. Lasky (and the other authors of this paper) in [14] has shown the importance of considering higher order modes in the calculation of memory and they explore the contribution of them. They have used the numerical relativity surrogate model NRSur7dq2 [15] which is valid more mass ratios $1 \leq q \equiv m_1/m_2 \leq 2$, dimensionless spins smaller than 0.8 and modes in between $2 \leq l \leq 4$. Figure below shows the periodic memory including higher order modes:

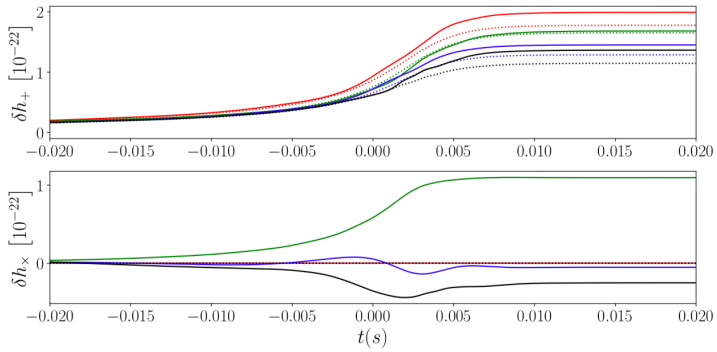

Figure 3.1: This figure is directly taken from [14]. Including higher-order oscillatory modes significantly affects the predicted memory. Comparison of the + (top panel) and × (bottom panel) polarization of the memory time series when using only the $l = |m| = 2$ oscillatory modes (dotted) and when using all modes with $l \leq 4$ (solid). The colors are for binaries as follows: red is equal-mass (q = 1) and non-spinning ($S_1 = S_2 = \vec{0}$), green is equal-mass with precessing spins ($S_{||} = 0, S_\perp = 0.8$), blue is unequal-mass and non-spinning, black is unequal-mass (q $\equiv m_1/m_2 = 2$) with precessing spins. In all cases, the late-time memory is different by O(10%) compared with the l $= |m| = 2$ only case and is larger for large mass ratios and large, precessing, spins. For non-spinning binaries, this is due to the excitation of higher-order modes during merger and ringdown. Ignoring the higher-order modes completely removes the predicted × polarized memory. The systems shown are edge-on ($\iota = \pi/2$,$\phi = 0$) with total mass, M = $60M_\odot$, at a luminosity distance, D_L = 400Mpc.

This figure is calculated for a binary of total masses of $60M_\odot$, distance of $400Mpc$ and zero polarization angle and $\pi/2$ inclination angle. Taking higher modes into account changes the result for memory at least by 10%. This increases for non-equal mass binaries and precessing binaries. Also in these cases the cross term of the memory does not vanish in higher modes.

There are two methods to compute non-linear memory: SXSmethod and Micheal's method [16] with integrating over the first derivative of h(t).

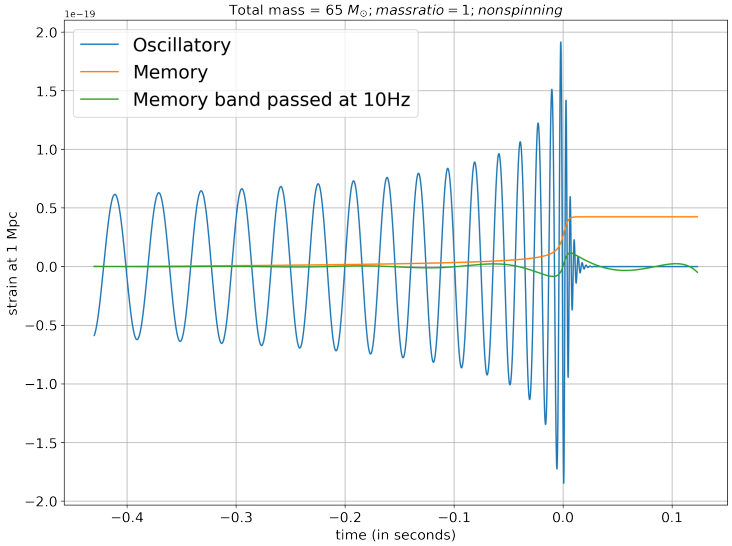

Figure 3.2: In blue is the wave form of a non-spinning binary system of equal mass together with the plot of its memory in orange. In green is when we band passed the memory at 10 Hz from which wave form is being generated which has a cycle.

Figure above shows the memory effect of a passing gravitational wave and the waveform itself. Memory is at its highest amplitude as the system merges, when the waveform reaches its most frequency. Then after the merger when the binary turned into one remnant massive object, the memory stays the same.

3.1 Dependence of non-linear memory on total mass

Non-linear memory depends on multiple characteristics of the system. Total mass is one of the features of the system that non-linear memory drastically depends on. One could plot the memory waveform for systems with various total mass and study the effect.

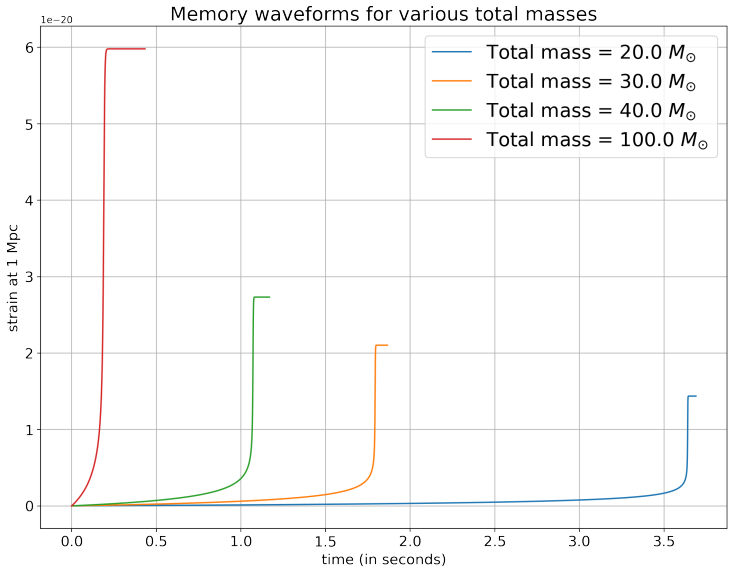

Figure 3.3: We plot the non-linear memory systems with different total mass. The mass ratio of these systems is one, and their inclination angle is zero.

As it's shown in figure above, the higher the total mass, the larger is the memory effect. Also systems with higher total mass merge faster than low-mass systems, therefore the memory plot peaks earlier in time for them.

3.2 Dependence of non-linear memory on mass-ratio

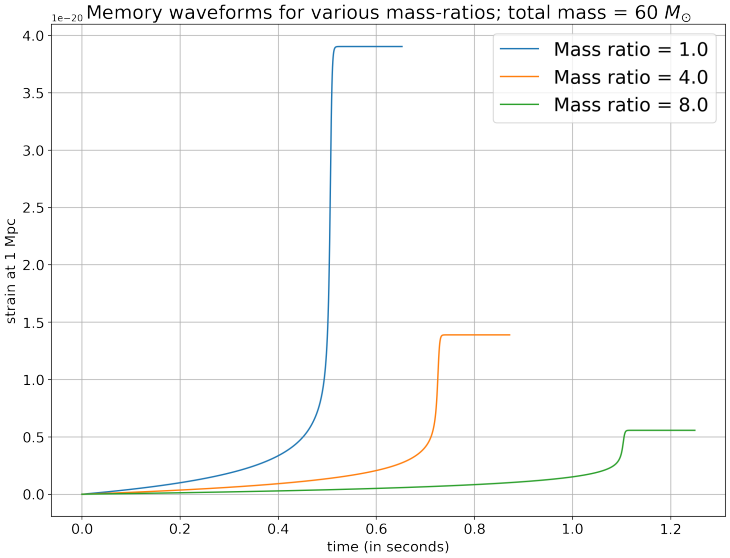

Figure 3.4: We plot the non-linear effect of three different non-spinning systems of total mass 60 $M_\odot$. The line in blue refers to the non-linear memory effect of a system with equal masses. The line in orange refers to a system of different masses, mass ratio being equal to four. The line in green refers to a system with mass ratio equal to eight.

The effect of mass ratio on non-linear memory is studied in the plot above. As one can conclude, the bigger the mass ratio, the smaller is the effect of non-linear memory. Systems with equal masses tend to leave a more significant memory effect

3.3 Dependence of non-linear memory on Aligned spins

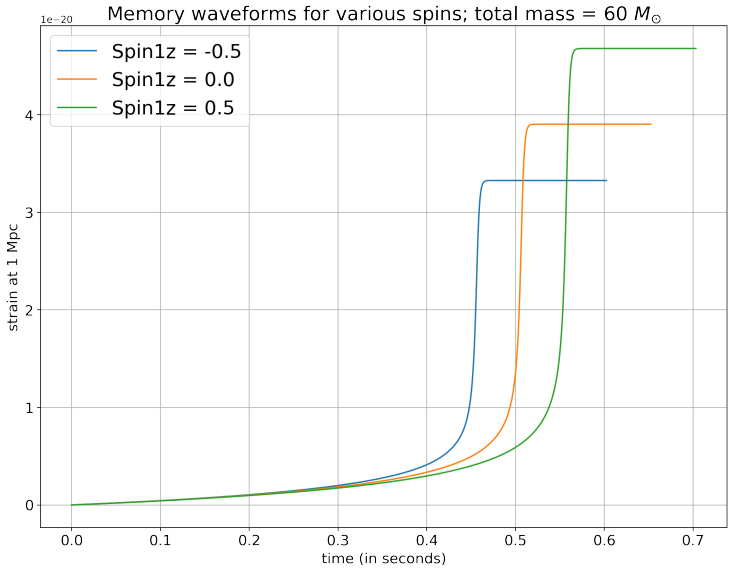

Figure 3.5: Here we plot the non-linear memory effect of three different systems. All have the total mass of 60 $M_\odot$. The line in blue refers to an equal mass system with a negative aligned spin, -0.5 in z direction. The line in orange refers to a similar system, but non-spinning. The line in green refers to a similar system as the other two, but with a positive aligned spin, 0.5 in z direction.

As it's represented in the plot above, the non-linear effect of aligned spinning system is greater than non-spinning, and the non-linear effect of non-spinning systems is greater than systems spinning in negative direction. Therefore it's easier to observe the memory effect of aligned spinning systems.

3.4 Dependence of memory on inclination angle

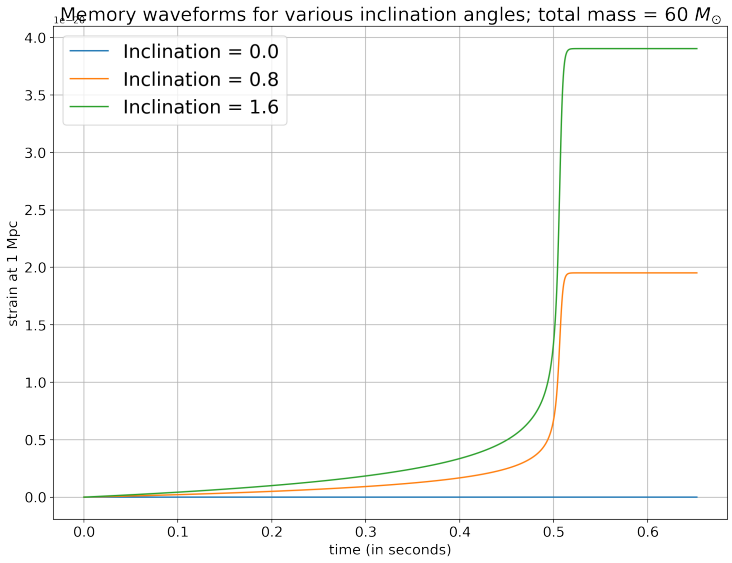

Figure 3.6: We plot the non-linear memory for non spinning systems with same masses, but different inclination angles. In blue is the memory of a binary system with zero inclination angle. The line in orange is for inclination angle equal to $\pi/4$ and the one in blue is for inclination angle equal to $\pi/2$.

The Zero inclination angle refers to the case where the l=2 , m=2 mode is the peak, and the memory is zero. Inclination angle of $\pi/2$ is for the case where (2,2) mode is negligible, therefore the memory is maximum.

Chapter 4

Inference of source parameters from BBH detectors

In order to extract physical properties out of the detected data, statistical and computational methodology come into use. One needs to estimate the physical parameters of the wave form model and take into account their uncertainties to eventually characterize the emitting source up to a good order of accuracy. There are some parameter estimation methods and wave form models. We want to go through the ones that has been used by LIGO and Virgo, in this part. The very first signal observed by the two LIGO observatories, LIGO- Livingston Observatory (L1) and LIGO-Hanford Observatory (H1), was analyzed using LAL Inference package of the LIGO Algorithm Library (LAL) software suite. [17] Some of the estimated physical parameters were the masses, spin, luminosity distance and sky position. GW150914 was detected then by estimating the corresponding masses as $36M_{\odot}$ and $29M_{\odot}$. [18]

One of the approaches to statistical inference is called Bayesian approach. Bayes' theorem relates the probability of an event to the prior knowledge of included conditions in that event. Bayesian approach is the application of Bayes' theorem. For instance, its application on two observable events A and B in terms of probabilities is as follows: [18]

$$\boldsymbol{P}(A|B) = \frac{\boldsymbol{P}(B|A)\boldsymbol{P}(A)}{\boldsymbol{P}(B)} = \frac{\boldsymbol{P}(B|A)\boldsymbol{P}(A)}{\boldsymbol{P}(B|A)\boldsymbol{P}(A) + \boldsymbol{P}(B|A^c)\boldsymbol{P}(A^c)} \tag{4.1}$$

Where $\boldsymbol{P}(B) \neq 0$. $\boldsymbol{P}(A|B)$ is the posterior probability of A given B is true, or the probability of event A occurring if B has occurred. $\boldsymbol{P}(A)$ is the prior probability, which is the probability of A happening without any other conditions. In other words, take $\boldsymbol{\theta} = (\theta_1, .., \theta_p)$ as parameters of the model and $\boldsymbol{d} = (d_1, .., d_n)$ as the observed data. The probability of the parameters of the

model before observing the data is called prior probability, $\pi(\boldsymbol{\theta})$, as opposed to posterior probability which is the uncertainty of the model parameters after the observation, $\boldsymbol{P}(\theta|d)$, the result we are looking for. The conditional probability, $\boldsymbol{P}(\boldsymbol{d}|\boldsymbol{\theta})$, is the probability of the data if the model is true, or the likelihood of the data to the model, $L(\boldsymbol{d}|\boldsymbol{\theta})$, the conditional probability density function. Using Bayes's theorem, one gets the following term for the posterior probability after the observation:

$$p(\boldsymbol{\theta}|\boldsymbol{d}) = \frac{L(\boldsymbol{d}|\boldsymbol{\theta})\pi(\boldsymbol{\theta})}{Z} = \frac{L(\boldsymbol{d}|\boldsymbol{\theta})\pi(\boldsymbol{\theta})}{\int L(\boldsymbol{d}|\boldsymbol{\theta})\pi(\boldsymbol{\theta})d\boldsymbol{\theta}} \propto L(\boldsymbol{d}|\boldsymbol{\theta})\pi(\boldsymbol{\theta}) \tag{4.2}$$

The approximation is valid since the denominator Z, which is the marginal likelihood, is just a normalization factor as it is not dependent on $\boldsymbol{\theta}$. However, it should be taken into account while comparing models. Let's bring the gravitational wave example. The data is made of K different time series detected by K interferometers, the one Advanced Virgo detector in Italy, the cryogenic detector KAGRA in Japan, the GEO 600 in Germany and two Advanced LIGO detectors in USA, $\boldsymbol{d} = (d^{(1)}, .., d^{(k)})$. Each $d^{(k)}$ is a time serie, $d^{(k)}(t)$ where $t = 1, ..., T$, T being the total number of measurements. T can be calculated by the multiplication of sampling frequency and the observing time , $T = f_s \times \tau_{obs}$. Δ_t is the time between each measurement. Now the gravitational wave data can be modeled by gravitational wave signals added to the interferometer noise:

$$d^{(k)}(t) = h^{(k)}(t|\theta) + n^{(k)}(t) \tag{4.3}$$

There are many noise sources causing this term, such as quantum, seismic, and thermal noise which is assumed to have zero mean value, wide sense stationary, and Gaussian with power spectral density (PSD); the distribution of the power of a signal in frequency domain.

PSD is a good tool to describe the second order properties of the time series. It is the Fourier transform of the auto-covariance function, $\gamma^{(k)}$, which calculated the covariance of a time serie with itself:

$$S^{(k)}(f) = \Sigma_{l=-\infty}^{\infty} \gamma^{(k)}(l) e^{-ilf} \tag{4.4}$$

There are some statistical methods to approximate the noise time series and GW signal parameters separately. The GW signal, $h^{(k)}(t|\theta)$, depends on variety of parameters such as compact binary masses, spins, their distance to earth and so on. Let's say GW signals depend on p parameters: $\boldsymbol{\theta} = \theta(\theta_1, ..., \theta_p)$. For binary inspiral signals, which is the focus of this section, the number of total parameters is fifteen with the prior $\boldsymbol{\pi}$. Assume the sky location of the binary is (α, δ) where δ is the elevation. The GW signal can be written as follows:

$$h^{(k)}(t|\boldsymbol{\theta}) = F_+^{(k)}(\alpha, \delta, \Psi) h_+(t|\boldsymbol{\theta}) + F_\times^{(k)}(\alpha, \delta, \Psi) h_\times(t|\boldsymbol{\theta}) \tag{4.5}$$

$F_{+,\times}$ is the response of the interferometer which is a function of the sky location of the binary and the GW polarization angle.

The sampling frequency of the time series is 16384 Hz for LIGO and 20 kHz for Virgo, however, it usually gets down sampled to 4096 Hz. Also it band pass filtered as the LIGO and Virgo detectors are sensitive to the frequency bands of 10 Hz to 5 kHz and 10 Hz to 5 KHz respectively and it is cut around for the known frequencies of instrumental noise.

The following is referred to as the Whittle likelihood which can be approximated from the exact Gaussian likelihood as follows:

$$L(\boldsymbol{d}|\boldsymbol{\theta}) = \prod_{k=1}^{\boldsymbol{K}} L(\boldsymbol{d}^{(k)}|\boldsymbol{\theta})$$

$$\propto \prod_{k=1}^{\boldsymbol{K}} e^{(-1/T)}(\tilde{\boldsymbol{d}}^{(k)} - \tilde{\boldsymbol{h}}^{(k)})^* \boldsymbol{S}^{(k)^{-1}}(\tilde{\boldsymbol{d}}^{(k)} - \tilde{\boldsymbol{h}}^{(k)})$$

$$\tilde{d}_j^{(k)} = \tilde{d}^{(k)}(f_j) = \Sigma_{t=1}^{T} d^{(k)}(t) e^{-itf_j} \tag{4.6}$$

Where $\tilde{\boldsymbol{d}}^{(k)}$ is the Fourier transform of the data. [18]

In eq. 4.6 the assumption that the observations are independent and they have stationary Gaussian errors with known PSD is taken into account. Therefore, one can write the total likelihood as the summation of each individual likelihood. $S^{(k)}$ is the PSD diagonal matrix at the Fourier frequencies $f_j = 2\pi j/T, j = 0, ..., N$ where $N = [(T-1)/2]$. The approximation refers to the fact that Whittle uses Gaussian likelihood to describe a non-Gaussian likelihood.

4.1 Signal to noise ratio (SNR)

In this section we want to compare the sensitivity of the anthena with the strength of the source and expected SNR, which measures the strength of the signal compared with the sources of potential noises. SNR is defined as the ratio of the power of the signal to the power of noise:

$$SNR = \frac{P_s}{P_n} \tag{4.7}$$

The signal received by a detector is a combination of a wave form, $h(t)$ and noise, $n(t)$. The aim is to find a simulated wave form, $q(t)$ which is optimal, meaning that has the best signal to noise ratio on average. Given a signal indicated by $x(t)$ which is the outcome of the detector, one can write the Fourier transform of it as [19]:

$$\tilde{s}(f) = \int_{-\infty}^{\infty} s(t) e^{2\pi i f t} dt \tag{4.8}$$

Take $s(t)$ the data observed by the detector, and assume it includes a signal $h_0(t)$ [20]:

$$s(t) = h_0(t) + n(t) \tag{4.9}$$

The aim is to extract signal parameters of a detected merger as accurately as possible. To do so, we begin with identifying parameter space regions which give the most consistent signal with the data, or they contain wave forms that have a good match with the data observed. This is part of the parameter estimation process. Therefore, we expect that the confidence regions in parameter space are regions with high match between signal and template. We want to derive an expression that gives the value of a match for a given confidence region at a given SNR.

We Taylor expand the signal in the parameter region to study the parameter extraction in leading order:

$$h(\theta) = h_0 + \theta^i h_i \tag{4.10}$$

The derivative of the wave form h with respect to the parameter θ_i is noted as $h_i = \partial_i h$. One can write down the following for the likelihood :

$$p(s|\theta)) \propto \exp\left\{-\frac{(s - h(\theta)|s - h(\theta))}{2}\right\} \tag{4.11}$$

One could substitute eq. 4.9 for s and use the Taylor expansion eq.4.10 to get:

$$p(s|\theta) \propto \exp\left\{-\frac{(n|n)}{2} + \theta_i(n|h_i) - \frac{\theta_i\theta_j(h_i|h_j)}{2}\right\} \tag{4.12}$$

Where the left hand side can be rewritten using Bayesian theory parameter estimation mentioned earlier:

$$p(s|\theta)) = p(\theta|s)p(\theta) \tag{4.13}$$

$p(\theta)$ is the prior probability distribution which we assume a uniform distribution The goal is to calculate the size of the confidence region od parameters, a region Θ which contains a total probability of p of a given posterior distribution.

$$p = \int_\Theta d\theta p(\theta|s) \tag{4.14}$$

To calculate the expected offset of the true parameters and the mean value from the posterior distributuin, we begin by calculating the mean of the parameter θ_i:

$$\langle\theta_i\rangle = \int d\theta\theta_i p(\theta|s) = (h_i|h_j)^{-1}(n|hj) \tag{4.15}$$

This equation shows that the mean of the posterior distribution will e offset from the true value because of the existence of noise. One an characterize this by evaluating the size of the error wave form:

$$h_E = h(\langle\theta_i\rangle) - h_0 \tag{4.16}$$

The expectation over different noise realization is then:

$$\langle h_E^2 \rangle_n = \langle (n|h_i)(h_i|h_j)(h)j|n) \rangle_n = k \tag{4.17}$$

Where k is the dimension of the parameter space. Therefore, one can claim that the amplitude of the difference of the best fit and the true signal is $\sqrt{k}$. One way to construct the confidence region is to calculate it using the Fisher approximation. After some calculation (See [20] for more detail), one reaches the following equation:

$$p(s|\theta)) \propto \exp\left\{ -\frac{1}{2}(\theta_i - \langle \theta_i \rangle)(h_i|h_j)(\theta_i - \langle \theta_j \rangle) \right\} \approx \exp\left\{ -\frac{1}{2}(|h(\theta) - h(\langle \theta \rangle)|^2) \right\} \tag{4.18}$$

Then using the definition of the confidence region, one can derive the following criterion for the minimum region that has the probability p of the posterior :

$$|h(\theta) - h(\langle \theta \rangle)|^2 < \chi_k^2(1-p) \tag{4.19}$$

Where the right hand side is the chi-square value which means that there is (1-p) probability of obtaining that value or higher. k detotes the number of parameters, for the case of aligned spin wave form, six parameters: the amplitude A, the phase ϕ, time t_c, M, mass ratio γ, and the effective total spin parameter χ. The amplitude of the difference between the best fit and the wave form is smaller than the threshold for all point within the confidence region. One can write the following expression for the match:

$$M(h(\theta), h(\langle \theta \rangle)) \geq 1 - \frac{\chi_k^2(1-p)}{2\rho^2} \tag{4.20}$$

All points in the parameter space that the match of them satisfies the above equation constructs the confidence region. To better understand this equation, we bring an example: Take a three dimensional parameter space, a confidence region of 90% for SNR 10:

$$M(h(\theta), h(< \theta >)) \geq 1 - \frac{3.12}{2\rho^2} \tag{4.21}$$

Which corresponds to a match of 0.97. The same match for a two dimensional parameter space and 90% confidence region gives $1 - 2.3/2\rho^2$, which is for SNR 9.

4.2 Match

To analyze the detected signals one needs to be able to regenerate them by simulations and find the best matching simulated wave form by changing the parameters of the parameter space. We call the wave forms of a physical source that are detected by gravitational wave detectors *true wave forms*, and we indicate them by h_T and the simulated wave form calculated by a theoretical model,

a *model wave form* indicated by h_M. h_M is used like a filter that passes through the whole data signal received and searches for the useful data since the data includes the wave form and plenty of different noises. Clearly, where the the model wave form fits to a certain part of the signal, that part is most likely a true wave form. The term 'fitting' must have a mathematical definition. This data analysis technique is called match filtering. The definition of the match between two wave forms, $h_1(f)$ and $h_2(f)$ is as follows [20]:

$$M(h_1, h_2) = max_{\Delta t, \Delta\phi} \frac{(h_2|h_2)}{|h_1||h_1|} \tag{4.22}$$

The inner product is defined as:

$$(h_1|h_2) = 4R_e \int_0^\infty \frac{h_1(f)h_2^*(f)}{S_n(f)df} \tag{4.23}$$

Where $S_n(f)$ is the power spectral density. Let's call the actual wave form that has been produced by a physical source, true wave form h_T and the model wave form that we use to look for the true wave form or signal in the detected data, h_M. We may use the normalized wave forms and split the model wave for in two parts, a part that is parallel to the true wave form (in the sense of defined inner product) and a part that is orthogonal to it, the error part:

$$\hat{h}_M = \sqrt{1 - x^2}\hat{h}_T + x\hat{h}_E \tag{4.24}$$

It is clear that the inner product of the true wave form with the error part of the model should give zero. The match between the two can be simplified as follows:

$$(h_M, h_T) = (1 - x^2)(h_T, h_T) + (h_E, h_T) = \sqrt{1 - x^2} \approx 1 - \frac{x^2}{2} \tag{4.25}$$

This shows that the match depends directly on the amplitude of the error part, x.

The template model bank used in GW search is built in a way that the match between any wave form parameter space and the nearest template is greater or equal to 97% therefore we won't lose more than $1 - 0.97^3 \approx 1 - 0.9 = 0.1$ or 10% of the data, of course assuming the template model are absolute physically correct wave forms. This is because the match of 97% means that the detector is sensitive to this percentage, which makes its sensitivity to the incoming data to 90% of the optimum volume. [20]

There is a python package, pycbc.filter package, which includes functions for this regard. The 'match' function from this package takes two wave forms as input and provides a number that indicates the percentage of matching of the two wave forms. The goal is to find the optimal wave form for a data

4.3 Degeneracies in BBH source parameters

The wave-forms detected by gravitational wave detectors are useful once one could study them, learn about the source which emits those gravitational waves.

One can learn about the parameters of the source using filters, by passing it through the data and finding the best match. Then the following question arises: Is it possible to have perfect matching yet having incorrect results? This would happen if the parameters are degenerate.

In this section, as mentioned before, the degeneracy between source parameters are examined. To do so, one needs to compare the wave forms of systems with different features, for instance a system of equal mass binary black holes with no spin compared with one without spin but with different masses. (discussed is section 3.2) This topic is consequential as it leads to better understanding the data detected by GW detectors. It may be the case that the received signal could be simulated by two different sets of parameters (physics). This is problematic for parameter estimation.

4.4 Mass-ratio spin degeneracy

The degeneracy between mass ratio and spin can be tested using the match filtering method. The so called degeneracy exists also for high mass binaries such as BBHs and goes on till the last stages of the binary evolution.

The following figure illustrates the matching between the two wave forms as a function of different mass ratios and total mass of the first BBH system.

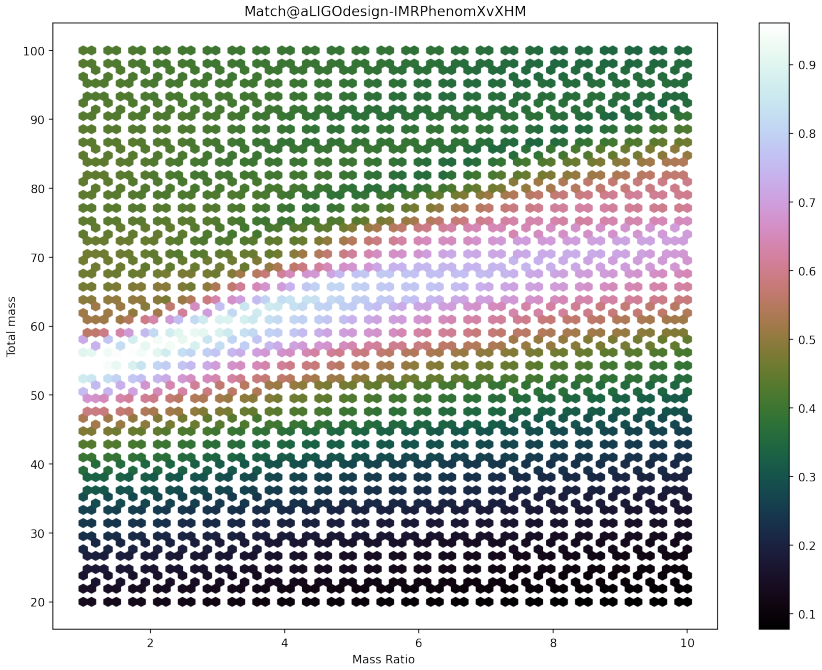

Figure 4.1: Mass ratio-spin degeneracy. The matching between a BBH system with masses 30 $M_{\odot}$ and aligned spin of 0.6 and another BBH system of different mass ratios and total masses with no spin.

It can be inferred from the figure that the matching can be over 0.9 for certain mass ratio and total masses. This illustrates the degeneracy between spin and mass ratio: Wave forms of a compact binary system with equal masses and aligned spin can be generated by a system with no spin but having different masses.

Chapter 5

Effect of non-linear memory on test of GR

5.1 Introduction to test of GR with gravitational wave Ligo/Virgo

An effective way to test a theory is to study its predictions and compare it with different models instead of either approving or ruling out the whole theory. Like this, one can see which features of a theory is confirmed through testing and which parts of it needs yet to be approved and what kind of observations need to be done to perform the testing [3]. Edington's idea [The Mathematical Theory of Relativity, by Arthur Stanley Eddington] of writing Schwarzschild metric in isotropic coordinates and adopting some new parameters in front of the different powers of Gm/rc^2 terms later became the famous "parametrized post Newtonian" formalism (PPN).

$$\begin{aligned} -g_{00} &= 1 - 2\frac{Gm}{rc^2} + 2\beta^{PPN}(\frac{Gm}{rc^2}) \\ g_{ij} &= \delta_{ij}(1 + \gamma^{PPN}\frac{Gm}{rc^2}) \end{aligned} \tag{5.1}$$

Which one gets to General relativity for β^{PPN}=γ^{PPN}=1. The constrains on these parameter's deviation from GR, $\beta^{PPN} - 1$ and $\gamma^{PPN} - 1$, which was calculated by contrasting the experimental results and GR predictions, are of the order 10^{-3} [21]. This confirms that the theory of GR is quite consistent with the experiments at the first post Newtonian order.

Binary pulsar observations are interesting systems to perform tests of GR. [21] The discovery of R.A. Hulse and J.H. Taylor in 1975 was an important start for this regard. They noticed that the pulsation period of the observed pulsar was 59 ms shorter than other pulsars known till then. Their work was the first massive object's gravitational interaction ever detected. [22] It contained two

neutron stars orbiting around one another which one of them was an observed pulsar with a highly eccentric orbit. As explained earlier, one can compare the predicted and measured relativistic phenomenon to test the theory of general relativity. GW damping is one of the first and most important phenomenons used to test GR. The back reaction of gravitational wave causes a change in Keplerian parameters, P_b , x and e, because it effects the angular momentum and orbital energy of the binary. The change of $x = a_p sin(i/c)$, the projected semi-major axis of the pulsar orbit, is yet smaller than the measurement precision, thus one can not observe the contractions of the orbit through x. Changes in eccentricity of orbit is also below the measurement precision. [23]

On the other hand, the orbital period is a good example as it changes significantly. What Taylor and Hulse realized, that the orbital period measured is less than the calculated period, confirms that gravitational radiation exists as the difference in orbital period is due to the gravitational wave emission of the binary system. [24]

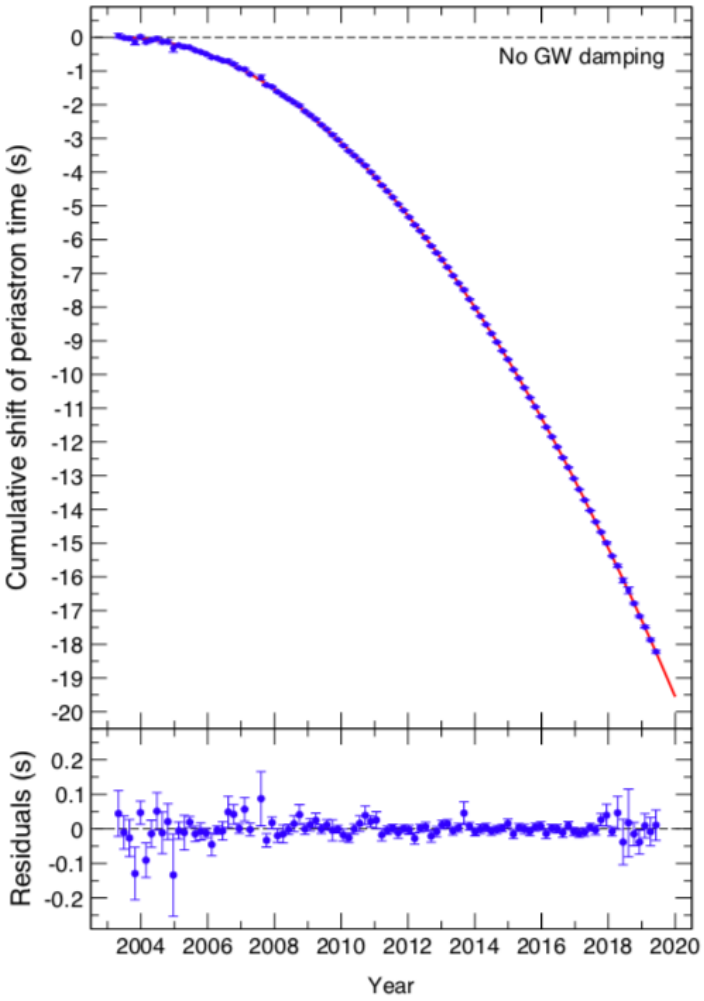

Figure 5.1: This figure is directly taken from [25]. Cumulative shift of the times of periastron passage relative to a non-dissipative model. Each data point covers a time span of 60 d. To each of these subsets, we fit a Keplerian orbit optimizing only for the orbital period and the time and angle of periastron passage. We include the advance of periastron, light- propagation effects, and the Einstein delay in the orbital model but keep the values fixed to those in Table IV. We plot the difference between the measured time of periastron and a periastron time near its discovery (i.e., MJD 52759.89, or 2003.33). The red curve in the top is the GR prediction based on the masses in Sec. VI B 1. The bottom shows the deviation from this prediction, characterized by a normalized.

The pulsar detection gives an incredible precision to the 0-th order post Newtonian expansion, as the detection started a long time ago and there is a greater amount of data. In pulsar detection objects are so far away to each other that1 the system is not in the relativistic merging phase. Therefore it gives a fairly good test for Newtonian regime. We will come back to this later.

General relativity predictions are consistent with cosmological measurements

and our solar-system experiments as well. But all these make no constrains on strong field regimes.

The detection of GW150914 binary black holes in 2015 by LIGO on the other hand provided a great opportunity to study the highly nonlinear, dynamical regime or strong field regime of gravity. GW signals of such merging evolves in three phases. The spiral of two compact object towards each other due to gravitational wave back reaction emission is called inspiral phase. Inspiral phase is not so complicated to approximate using PN formalism or effective one body solution. One can use analytical approaches to study this phase because it's non-relativistic, despite the next phase, merger. To approximate merger, one needs to adopt numerical calculations of Einstein field equations using supercomputers. The last phase is called ring down, where the remnant merged object starts to settle down by GW emission. This phase is well approximated by black hole perturbation theory. [26] The detection of GW150914 covers all three stages, the inspiral, the merger and the ring down of vacuum black holes. Before this detection, even the most relativistic binary observations measured a rather small rate for the orbital period changes due to the radiation of energy and angular momentum, the rate of these observations was of the order $\dot{P} = -10^{-12} - 10^{-14}$. For instance, the orbital velocity relative to the speed of light for for the pulsar observation J0737-3039 is $v/c = 2 \times 10^{-3}$ and the system coalesces in around $85Myr$. But the rate of orbital period changes for the GW150914 observation is of the order $\dot{P} = -0.1$ at frequency of 30 Hz and $\dot{P} = -1$ at the frequency of 132 Hz. The speed relative to the speed of light before the merger increases up to about $v/c = 0.5$ [27] Therefore, the GW150914 observation gives us enough tools to test GR on relativistic strong field regime and learn about emitted GWs after generating a new merged object through a two body motion problem and its merging. After several studies on GW150914, it was clear that the hypothesis of GW150914 being the waveform emitted by two spiraling black holes which will merge together and form one rotating black hole, is indeed correct. It worth mentioning that the mass and spin of the system in the low frequency and high frequency phases are consistent with the general relativity solution of this system, the dynamic of the process is in the scheme of vacuum Einstein field equations. [27]

The more recent discovery of the Advanced LIGO and Advanced Virgo, in 2017, is the emission of binary neutron stars system. Detection of gravitational waves emitted by this system, GW170817, performs tests of GR in presence of matter. The two neutron stars orbit around each other till merger happens. The newly made bigger neutron star starts wobbling and emits GWs of higher frequency (higher than the sensitivity of current detectors). Then after a rather small amount of time the remnant neutron star collapses into a black hole. The gamma ray bursts of the after-made black home were also observed in this observation run, GRB 170817A, detection of short-duration gamma-ray burst (SGRB). These two sets of indicating waves were detected within a second apart from each other. The distance they travelled was 40 Mpc which is about 160×10^6 light years. Therefore, this particular observation provides us with strong constraints on the difference between the speed of light and the speed

of GWs. The speed of GWs has significant importance on fundamental physics such that the constraints applied on it by the second detection GW170817 run ruled out many theories about the nature of dark energy. Also it is worth mentioning that the idea of massive gravitons were put in danger after this detection because GWs travel at the speed of light or at least very close to it. Such important detection of course needs to be as accurate as possible, therefore all the involved parameters such as the distance of the detector to the galaxy who is emitting the waves or the travel time delay was considered generously in favour of broadening the range of constraints. For instance if the instruments were so bad that the measurements had big systematic errors, thus the travel time difference was 300s instead of 1s. Eventually, the broadest range for the ratio of the relative speed of EM waves and GWs to the speed of EM wave is:

$$-3 \times 10^{-15} \leq \frac{\Delta v}{v_{EM}} \leq +7 \times 10^{-16} \tag{5.2}$$

Where $\Delta v = v_{GW} - v_{EM}$. Following approximation was taken into account:

$$\frac{\Delta v}{v_{EM}} \approx v_{EM} \frac{\Delta t}{D} \tag{5.3}$$

Which is yet extremely exact. This ruled out five dark energy models such as Horndeski model, Beyond Horndeski model, Host and DHost models. Also any massive gravity models which deals with tensorial perturbations were ruled out.

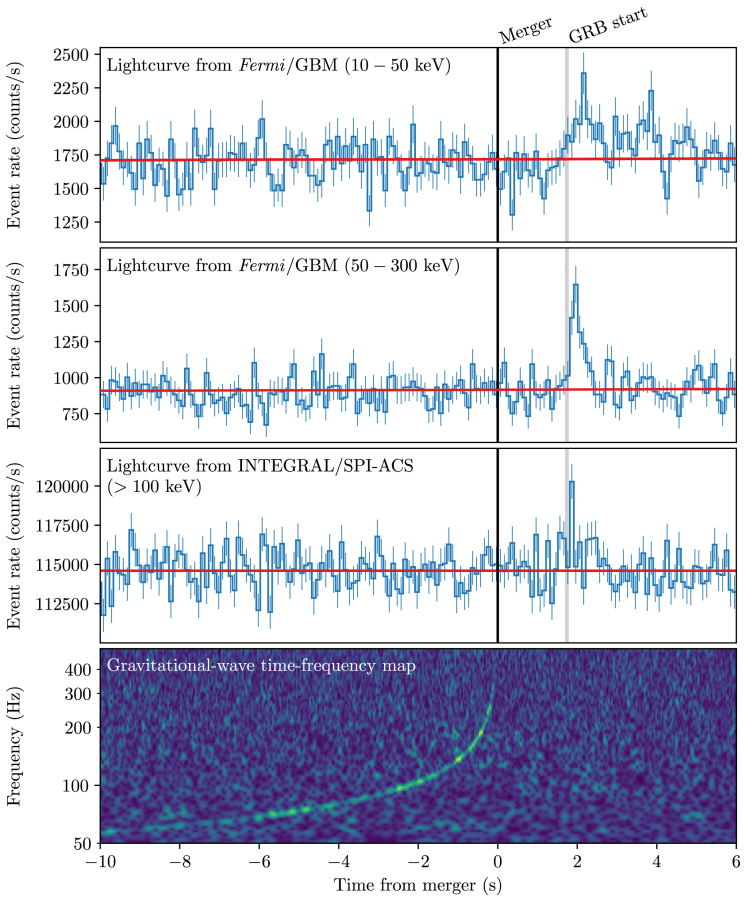

Figure 5.2: This figure is directly taken from [28]. The joint, multi-messenger detection of GW170817 and GRB 170817A. Top: The summed GBM light curve for sodium iodide (NaI) detectors 1, 2, and 5 for GRB 170817A between 10 and 50 keV, matching the 100 ms time bins of SPI-ACS data. The background estimate from Goldstein et al. (2016) is overlaid in red. Second: The same as the top panel but in the 50–300 keV energy range. Third: The SPI-ACS light curve with the energy range starting approximately at 100 keV and with a high energy limit of least 80MeV. Bottom: The time-frequency map of GW170817 was obtained by coherently combining LIGO-Hanford and LIGO-Livingston data. All times here are referenced to the GW170817 trigger time TGW. 0

In the figure above [28], one can see that the gamma ray peak happens within a few seconds after the GW peak. (The frequency of GW signals increases as it gets closer to the merger until it passes the limit of sensitivity of the detectors, which is why the peak is not visible in the graph.)

One of the other important differences between this test and the one done in 2015 on BBHs is that here one needs to take the tidal deformabilities of neutron stars into account in the wave form models. The merger and ringdown regimes are also different among the two. Finite size effects must be considered in modeling binary neutron stars. [29]

The first two observations of Ligo and Virgo detectors were consistent with

wave forms of Binary black holes and binary neutron stars. The third observing run of Ligo and Virgo however was dedicated to the detection of signals emitted by a system of neutron star-black hole, GW200115-042309. While testing GR, one has to know what pilar of GR is being tested. Is it about the assumption that the theory is Lorentz invariant? Is it the equivalence principle or is it about the description of the degrees of freedom in GR? So one needs to test each part separately. Comparing different tests of GR with each other is almost impossible.

Tests done on these detected signals includes tests on whether signals are consistent with the data, tests on remnant object of the merger and see if it satisfies the black hole ring down hypothesis, and search for post merger echos. [26]

There are different methods used to model GW signals emitted from different stages. The inspiral stage can be approximated by analytical formalism such as effective one body problem or post Newtonian approximations. These methods won't work as the system gets closer and closer to the merger as it becomes highly relativistic. To describe the system accurately one needs to numerically solve Einstein Field equations using numerical relativity method by supercomputers. After the coalescence, as mentioned earlier, system undergoes the ringdown phase which is well approximated by black hole perturbation theory. Tests of GWTC-3 mainly uses the observed signals to test these approaches. [26]

One of the analyses that was done in GWTC-3 was the 'Generic Modifications'. GW signals can change in presence of additional fields or stronger curvature as binary's binding energy and angular momentum flux changes [24]. This suggests alternative theories for general relativity or modifications. This part of analyses is dedicated to the deviations from GR. As explained above, PN approximation is used to analyse the inspiraling phase of GW signals which is a perturbative theory using the powers of v/c, nPN orders. The coefficients of different orders of v/c are uniquely specified in GR, given the intrinsic parameters of the binary, masses and the spins. So the perturbative expansion of early inspiral phase in GR is determined. Therefore it is not unusual to think of these coefficients as measurable parameters of the waveform and use it as a consistency test of GR. Bounds on deviations of these parameters can be set using low-mass inspiral dominated events. [26]

For each post Newtonian order, 0 , 1.5, 2, 2.5 and so on, zero would be mean no deviation from GR and there will be an upper limit on their deviation.

The constraints depend upon how long a theory is being tested, in this case, how many orbits has been detected. Having a more accurate test is a matter of observing a system for a longer amount of time. It depends on the number of clear orbits that we see- for instance even though in BNS system much more orbits were detected compared to BBH system, provided worse constraints because the signals were in a weaker signal strength. In the double pulsar detection, the evolution of a binary system is being detected. This detection has provide us with sixty years of data received from many double pulsar systems. As the pulsars are too far away from each other and their orbiting speed is not

comparable by the speed of light, v/c is very small, their orbit is Newtonian orbit according to GR Newtonian orbit, which is a decaying orbit. Thus, one would expect that the signals coming from such system would perfectly fit in the Newtonian regime of general relativity. As shown in figure 5.3 [23], the upper limit set by double pulsar detection on the zeroth order is quite close to zero. The reason of such great constraint on the zeroth order compared to BBH or BNS systems- three to four order of magnitude difference - is that the detection of binary pulsars has been going on for sixty years now providing a lot more detected orbits than BBH or BNS systems- relativistic systems- detection which take only a few milliseconds. Therefore, one can conclude that GR is a great theory for Newtonian regime. However, binary pulsars are not so good for setting constraints on higher post Newtonian orders as they are within a non-relativistic regime. For instance, the 0.5−th order, Ligo/Virgo detection has led to a comparable constraint with double pulsar detection. Because the double pulsar system is not even in strong field and their strong field signal strength is very weak. Eventually, the competition ends at the first order, where binary pulsars give results of hundred times worse than Ligo/Virgo detection. It is worth mentioning that the Hulse-Taylor pulsar detection did not give any probe the 0.5 or 1 PN because they were too far apart and too weak in these higher orders than zero. But the reason there is a constraint on these orders by double pulsar detection is the many more other systems that were detected and are closer to each other than the Hulse-Taylor pulsar system, therefore, emitted stronger signals.

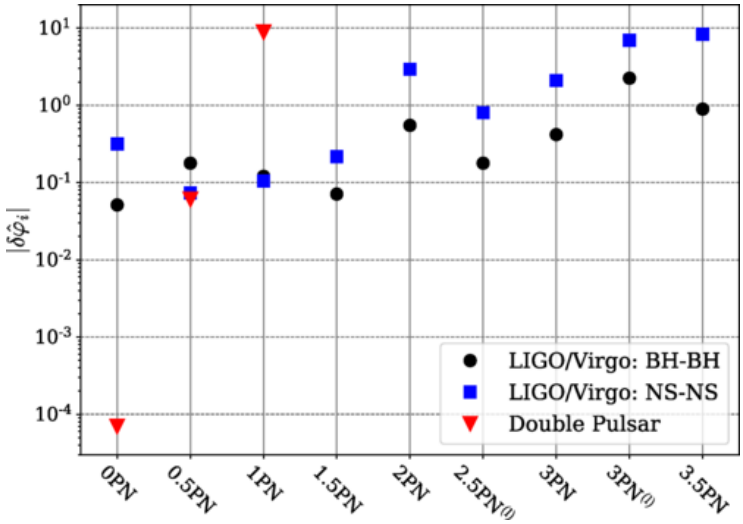

Figure 5.3: This figure is directly taken from [23]. -90% upper bounds on the magnitude of the parameterised test coefficients from -1 PN to 3.5 PN order as discussed in sec. 4.2. Bounds marked by blue diamonds were obtained with a pipeline based on SEOB waveform combining all eligible events from O1, O2 and O3.Filled (unfilled) gray triabgles mark analogous results obtained with GWTC-2 data 11 using SEOB (Phenom)models. Horizontal stripes indicate constraints obtained with individual events, with bluer (redder) colors representing lower (higher) total mass events.

So this plot indicates how strong is the double pulsar system for 0-PN. Thanks to this detection we know now that in a very weak field, GR is a really good theory. Bus as the system goes into stronger gravity, stronger curvatures or stronger velocity, the constraints gets less and that is where the direct detection of gravitational waves play an important role to set constraints.

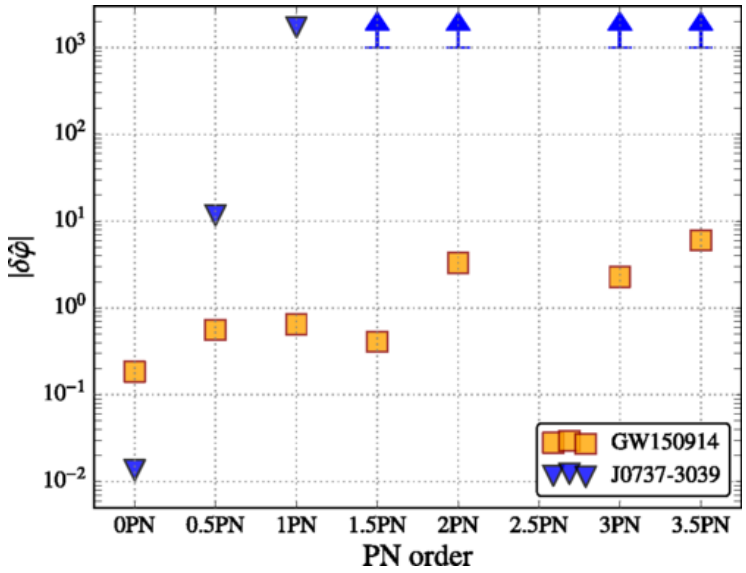

Figure 5.4: This figure is directly taken from [23]. 90% upper bounds on the magnitude of the parameterized test coefficients discussed in Sec. V A. The bounds were obtained with a pipeline based on the model SEOBNRv4 ROM, combining all eligible GWTC-3 events, under the assumption that deviations take the same value for all the events. Filled gray diamonds mark analogous results obtained with GWTC-2 data [11]; in this case, we also show bounds obtained with a pipeline based on IMRPhenomPv2,that are marked by unfilled black diamonds. Horizontal stripes indicate constraints obtained with individual events, with cold (warm) colors representing low (high) total mass events. The left and right panel show constraints on PN deformation coefficients, from -1PN to 3.5PN order. The best improvement with respect to the GWTC-2 bounds is achieved for the -1PN term, thanks ot the inclusion of the NSBH candidate GW200115 042309.

Figure 5.5 shows the 90% upper bounds on different PN order coefficients by GWTC-3. One can notice an improve in 0.5 order compared to the detection of BBH, in figure 5.4, which was above 10^{-1} and now is below 10^{-1}.

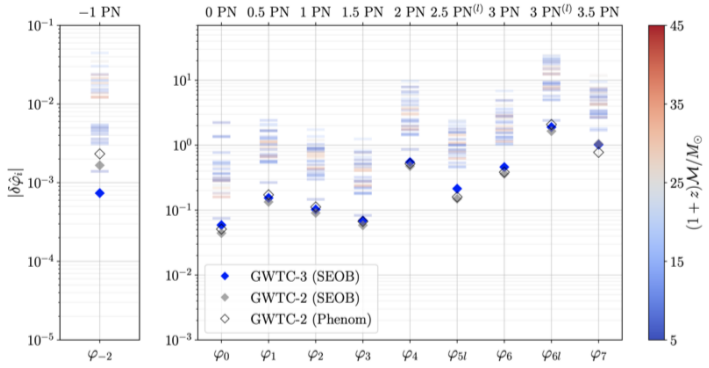

Figure 5.5: This figure is directly taken from [30]. −90% upper bounds on the magnitude of the parameterized test coefficients discussed in Sec. V A. The bounds were obtained with a pipeline based on the model SEOBNRv4 ROM, combining all eligible GWTC-3 events, under the assumption that deviations take the same value for all the events. Filled gray diamonds mark analogous results obtained with GWTC-2 data [11]; in this case, we also show bounds obtained with a pipeline based on IMRPhenomPv2, that are marked by unfilled black diamonds. Horizontal stripes indicate constraints obtained with individual events, with cold (warm) colors representing low (high) total mass events. The left and right panel show constraints on PN deformation coefficients, from -1PN to 3.5PN order. The best improvement with respect to the GWTC-2 bounds is achieved for the -1PN term, thanks ot the inclusion of the NSBH candidate GW200115 042309.

The bounds on PN parameters are shown in figure 5.5.

For each post Newtonian order, 0 , 1.5, 2, 2.5 and so on, zero would be mean no deviation from GR and there will be an upper limit on their deviation. As shown in figure 5.5, the best constraint is on zeroth order.

5.2 Parameterized test of General Relativity with Gravitational Waves

Parameterized test of general relativity (TGR), provides a great tool to test the theory in strong field regime, such as inspiraling compact binary, by constraining deviations of the post-Newtonian coefficients which represents the evolution of GW phase during inspiral. The goal of the next two sections is to investigate the impact of non-linear memory on the parameterized tests of GR and study the systematic biases due to the assumption of zero non-linear memory for a system. The theory of GR has been well approved in weak field regime and strong field regime thanks to many experiments and wave-form models that have been developed within GR. Mostly for GWs in different stages of a binary, which relates us to a more dynamical and strong field regime, since nonlinear effects are dominant. However, such models are less popular among alternative theories specially for merger and ring down phases which are highly relativistic and non-linear. Noting that solving two body problem is difficult even within GR, one can predict that it wouldn't be practical to solve it in alternative theories. One way is to compare GW signals with wave-form models that have

been developed by parametrically deviated GR and not full GR. In this framework, the inspiral part of the frequency domain of GW phase is parameterized by non-GR deviation parameters, which are added to each post-Newtonian order as free parameters. Measuring these deviations which get accumulated over many GW cycles, gives us a constraint on potential deviations of GR.

The main purpose of this section is to study the the effect of non-linear memory on the parameterized tests of GR if the binary is modeled using wave-forms without taking non-linear memory into account. Understanding the amount of bias that will affect the parameter estimation due to un-modeled non-linear memory is vital to have a remarkable TGR. A similar study has been done in [31] for eccentricity. [32] Shows the significant systematic biases in parameters that occurs due to modeling eccentric binaries by quasi-circular waveforms. Systematic errors exceeded the statistical errors considering the neglect of high post Newtonian order terms. It's worth mentioning that systematic errors despite statistical errors are independent of signal to noise ratio (SNR). Since statistical errors inversely depend on SNR, in high SNR sources, the systematic errors easily dominate statistical errors. The systematic biases affect the intrinsic parameter estimation of the system such as the masses and spins. To study this effect, we take the standard PN waveform in frequency domain and modify it by TGR deformation parameters.

GW signals measured in detectors can be expressed by the summation of the two polarization states in GR:

$$h(t) = F_+ h_+(t) + F_\times h_\times(t) \tag{5.4}$$

F_+ and $F_\times$ are called the antenna pattern functions which depend on the sky location of the source and the inclination angle,Ψ. One can write eq.5.4 using stationary phase approximation and Fourier transform it:

$$\tilde{h}(f) = \mathcal{A} e^{i\Psi(f)} = \hat{\mathcal{A}} f^{-7/6} e^{i\Psi(f)} \tag{5.5}$$

The amplitude parameter can be averaged over the inclination angle and antenna function:

$$\hat{\mathcal{A}} = \frac{1}{\sqrt{30}\pi^{2/3}} \frac{\sqrt{\eta} M^{5/6} (1+z)^{5/6}}{d_L} \tag{5.6}$$

$$\begin{aligned} M &= m_1 + m_2 \\ \eta &= \frac{m_1 m_2}{M} \end{aligned} \tag{5.7}$$

And z is the source redshift and d_L is the luminosity distance to the source. In PN theory one can expand the phase in powers of the relative orbital velocity:

$$\begin{aligned} \Psi(f) = 2\pi f t_c + \phi_c + \frac{3}{128\eta v^5} \Sigma_k \varphi_k v^k + \varphi_k^{log} v^k ln v) \\ v = [\pi M (1+z) f]^{1/3} \end{aligned} \tag{5.8}$$

t_c and ϕ_c are the time and phase of the coalescence. The summation index k varies over (-2,0,2,3,4,6,7) which indicate the $k/2$-th PN order. Each order is a function of intrinsic parameters of the system like mass ratio or the dimensionless spin $\mathcal{X}_{1,2}$ which are known for GR if the values of η, $\mathcal{X}_1$ and $\mathcal{X}_2$ are determined. The deviation from GR is defined as follows:

$$\begin{aligned} \varphi_k &\longrightarrow \varphi_k^{GR}(1+\delta\hat{\varphi}_k) \\ \varphi_k^{log} &\longrightarrow \varphi_k^{GR,log}(1+\delta\hat{\varphi}_k^{log}) \end{aligned} \tag{5.9}$$

We can use this and eq.5.8 to model a systematic bias in parameters due to non-linear memory and alter it to:

$$\Psi(f) \longrightarrow \Psi(f)^{TGR} + \alpha\delta\Psi(f)^{non-linear} \tag{5.10}$$

It's worth mentioning that GW detectors are more sensitive to GW phase than amplitude, therefore small corrections to the amplitude due to non-linear memory can be neglected.

5.3 Effect of non-linear memory on test of general relativity

As discussed before, memory has a permanent effect on the relative distance between two freely falling test masses, by inducing monotonically increasing GW strain that is due to strong field general relativistic effects. In this section we explore the effect of neglecting non-linear memory while performing various tests of GR. Indeed the memory will add up to the residue test of GR over time which lead to the detection of memory [33]. We discuss here what impact the single event tests of GR will have when one ignores the memory contribution.

5.3.1 Impact on generic parameterized test of GR

The most general parameterized test of GR is discussed before. This parameterisation is used to test GR not only with gravitational waves but also with Double Neutron Star tests with pulsar timing. There are several parameters which can be added to the various terms mimicking the post-Newtonian corrections and hence these terms become relevant only in the case of the black holes coming very close to each other (i.e. strong gravity regime). The memory also peaks at the merger time and hence one can intuitively conclude that memory will have significant contribution to these tests of GR.

In figure 5.6 we show how the additional GR effect compares with the memory. To do this we define two residues, the first one being the beyond GR residue which is simply the GR waveform, $h_{GR}(t)$, subtracted from the beyond GR waveform, $h_{bGR}(t)$, so the beyond GR residue is $h_{GR}(t) - h_{bGR}(t)$. The other residue is called memory residue, which is defined as $h_{GR}(t) - h_{GR}^{memory}(t)$. Here, $h_{GR}^{memory}(t)$ includes both the oscillatory and the memory part of the GR

signal. As expected and mentioned before we notice that the memory residue and the beyond GR residue peak around the merger of the event but it should be noticed that the morphology of the memory waveform is very different than the beyond GR waveform as the memory waveform will be at much lower frequency as compared to the one from the beyond GR contribution.

Further, one can imagine that memory contribution can become more similar to the beyond GR when one goes to higher masses. This can be due to the fact that the oscillatory signal to which the beyond GR corrections are defined will also have lower frequency if the masses are heavier. However, it should be noted that while that happens the amplitude of memory decreases in the sensitivity band of the detectors as the total mass of the system increases since the memory goes to even lower frequencies.

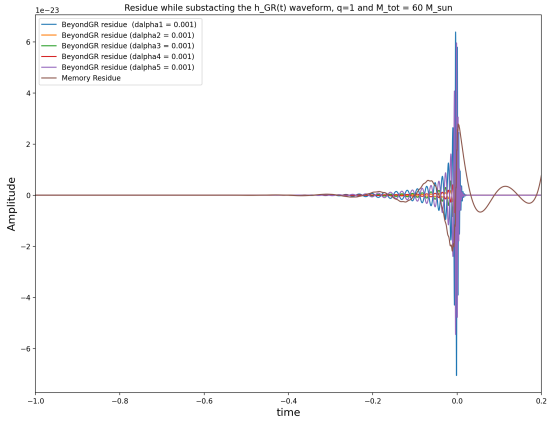

(a) Beyond GR parameter $\delta\alpha$

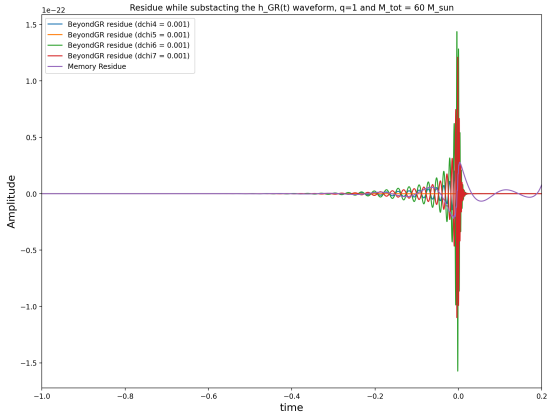

(b) Beyond GR parameter $\delta\chi$

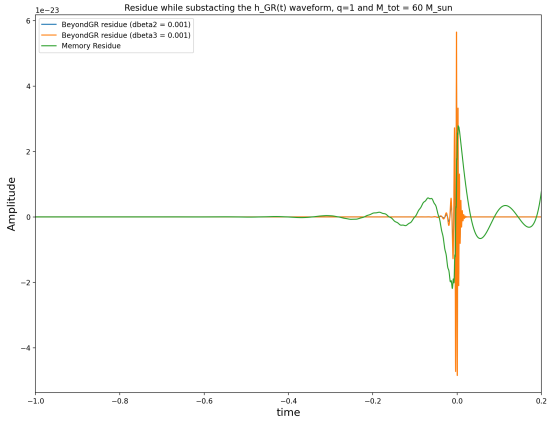

(c) Beyond GR parameter $\delta\beta$

Figure 5.6: The residues with respect to the GR oscillatory waveform are plotted here for various beyond GR parameters and non-linear memory. The system chosen here has total mass of $60M_{\odot}$, mass ratio of unity and is a spinless system mimicking the first detection, GW150914. The residues of the beyond GR parameters are clearly at much higher frequency than the memory waveforms which is expected.

In figure 5.7 we show the matches between the memory residue and the beyond GR residue as a function of total mass and spins. The matches between the residues is a good metric to measure the confusion of the memory signal with beyond GR corrections. The higher the match, the better memory is mimicking the effects of beyond GR. However, the maximum matches only reach up to 0.45 for the expected total masses in the LIGO-Virgo-KAGRA band. This shows that the memory signal is quite orthogonal to the generic parameterised tests of GR which are widely used and the effect of not adding non-linear memory to such tests will likely be non significant.

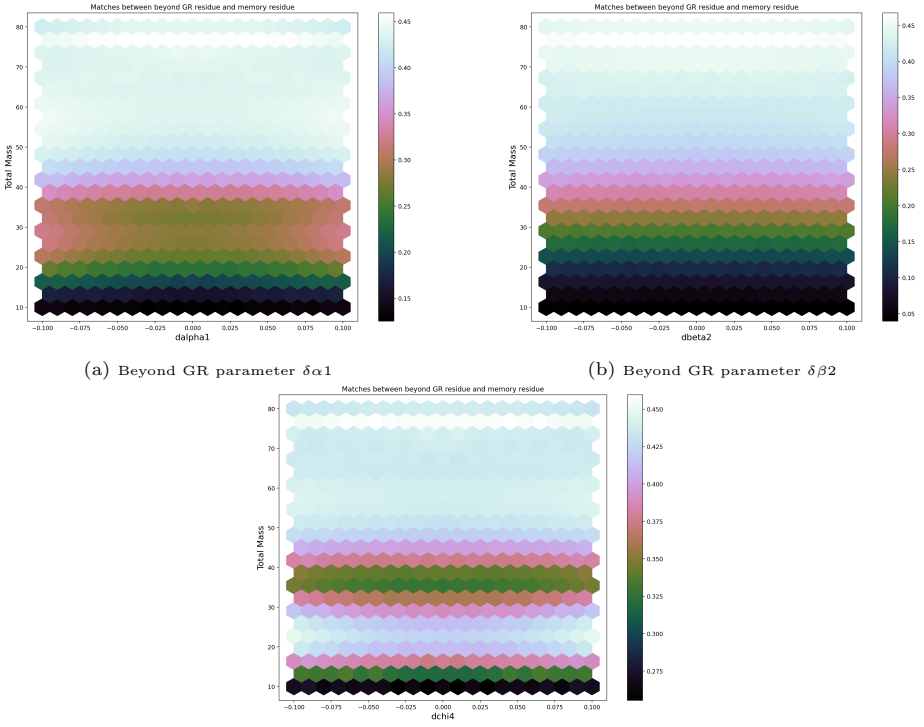

(a) Beyond GR parameter $\delta\alpha 1$

(b) Beyond GR parameter $\delta\beta 2$

(c) Beyond GR parameter $\delta\chi 4$

Figure 5.7: Here we show the variation of the matches between various beyond GR residue and memory as a function of total mass. As the mass increases the memory residue becomes more similar to the beyond GR residue. This is due to the fact that with higher total mass the beyond GR residue has lower frequency which becomes more similar to the memory residue. However, the matches are always less than 0.5 and hence memory is not truly mimicking the beyond GR residues.

5.3.2 Impact on inspiral merger ringdown tests

In this section we assess the impact of ignoring non-linear memory on the various tests of GR which involves looking at the inspiral and the merger ringdown part of the signal separately. Examples include inspiral-merger-ringdown consistency test and area theorem test. The way these tests are performed is by noting the end of inspiral part of the signal which is defined at the MECO (minimum energy

circular orbit) frequency detailed in this [34]. Temporally, memory occurs at the merger times but in frequency memory goes with the inspiral part of the signal. To test the effect that memory has on the inspiral part of the signal below the MECO frequency, we again perform the match study.

In figure 5.8 we study the mismatches (1-match) between the inspiral waveforms with and without memory. For the systems with low masses the mismatches are larger. This is expected as the memory contribution will be spread out over the full inspiral and the mismatches will be integrated. For heavier systems till around total mass of 50 $M_{\odot}$ the trend is linear, beyond that the mismatches again begin to increase. This is due to the fact that the inspiral signal in the band is very short and the addition of memory starts to affect it significantly again.

However it should be noted that the mismatches are extremely low, around 10^{-6}, and the effect of memory will be negligible for such systems as well.

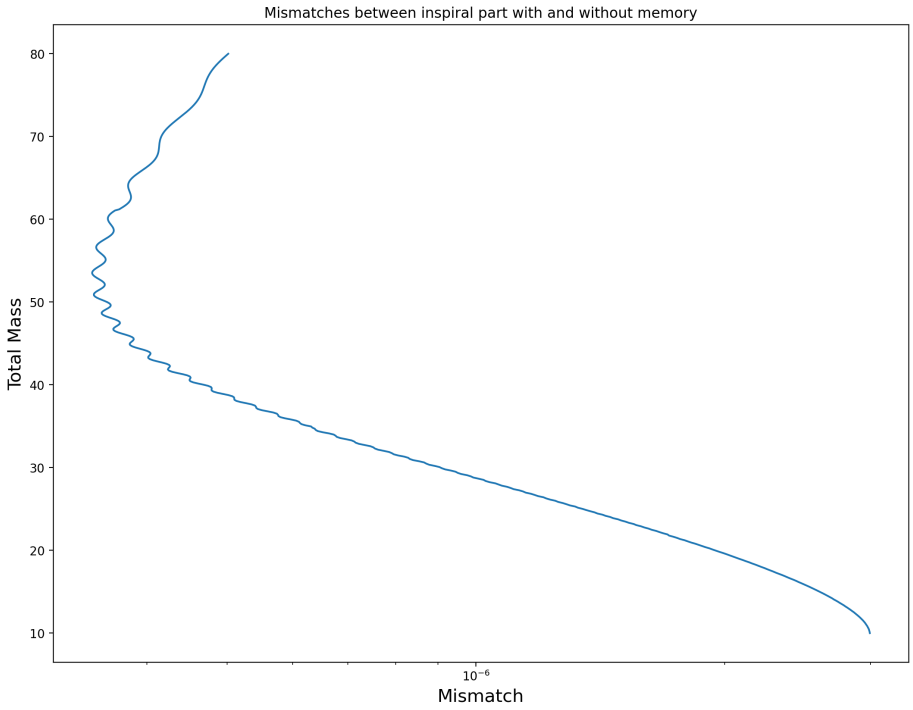

Figure 5.8: The mismatch (1-match) is plotted as a function of total mass for the inspiral part of the signal. The mismatches are negligible for most of the parameter space.

Chapter 6

Conclusions

h_+ $h_\times$ In this thesis I have presented various aspects of non-linear memory and in particular studied the effect of neglecting non-linear memory on the test of GR using the data of current generation ground based detectors.

We assessed the contribution of non-linear memory on the tests of general relativity and found that it's highly unlikely that memory will have an impact on the tests of general relativity involving single events for the current generation of interferometers. We looked at the generic parameterised tests where the morphology of memory signal is significantly different than the waveforms of proposed deviations from GR. In the case of inspiral merger ringdown consistency tests, we found that memory will have very low impact on the inspiral part of the signal if the total mass of the system is very low.

In the future with the third generation of interferometers there can be multiple events with very high signal to noise ratio. In that case non-linear memory can have some impact on the test of GR but until then the current tests of GR are safe when ignoring memory.

Bibliography

[1] Bernard F Schutz and Franco Ricci. Gravitational Waves, Sources, and Detectors. 5 2010.

[2] Alessandra Buonanno and Bangalore Sathyaprakash. Sources of gravitational waves: Theory and observations. 10 2014.

[3] R. Abbott et al. Tests of General Relativity with GWTC-3. 12 2021.

[4] B. P. Abbott et al. Prospects for observing and localizing gravitational-wave transients with Advanced LIGO, Advanced Virgo and KAGRA. *Living Rev. Rel.*, 21(1):3, 2018.

[5] B. P. Abbott et al. GWTC-1: A Gravitational-Wave Transient Catalog of Compact Binary Mergers Observed by LIGO and Virgo during the First and Second Observing Runs. *Phys. Rev. X*, 9(3):031040, 2019.

[6] R. Abbott et al. GWTC-3: Compact Binary Coalescences Observed by LIGO and Virgo During the Second Part of the Third Observing Run. 11 2021.

[7]

[8] Marc Favata. Nonlinear gravitational-wave memory from binary black hole mergers. *Astrophys. J. Lett.*, 696:L159–L162, 2009.

[9] Ulrich Sperhake. The numerical relativity breakthrough for binary black holes. *Classical and Quantum Gravity*, 32(12):124011, jun 2015.

[10] Luc Blanchet. Gravitational radiation from post-Newtonian sources and inspiralling compact binaries. *Living Rev. Rel.*, 9:4, 2006.

[11] Keefe Mitman, Jordan Moxon, Mark A. Scheel, Saul A. Teukolsky, Michael Boyle, Nils Deppe, Lawrence E. Kidder, and William Throwe. Computation of displacement and spin gravitational memory in numerical relativity. *Phys. Rev. D*, 102(10):104007, 2020.

[12] David A. Nichols. Spin memory effect for compact binaries in the post-Newtonian approximation. *Phys. Rev. D*, 95(8):084048, 2017.

[13] Y. B. Zel'dovich and A. G. Polnarev. Radiation of gravitational waves by a cluster of superdense stars. *Sov. Astron.*, 18:17, 1974.

[14] Colm Talbot, Eric Thrane, Paul D. Lasky, and Fuhui Lin. Gravitational-wave memory: Waveforms and phenomenology. *Physical Review D*, 98(6), sep 2018.

[15] Jonathan Blackman, Scott E. Field, Mark A. Scheel, Chad R. Galley, Christian D. Ott, Michael Boyle, Lawrence E. Kidder, Harald P. Pfeiffer, and Béla Szilágyi. Numerical relativity waveform surrogate model for generically precessing binary black hole mergers. *Phys. Rev. D*, 96:024058, Jul 2017.

[16] Michael Ebersold and Shubhanshu Tiwari. Search for nonlinear memory from subsolar mass compact binary mergers. *Physical Review D*, 101(10), may 2020.

[17] J. Veitch, V. Raymond, B. Farr, W. Farr, P. Graff, S. Vitale, B. Aylott, K. Blackburn, N. Christensen, M. Coughlin, W. Del Pozzo, F. Feroz, J. Gair, C.-J. Haster, V. Kalogera, T. Littenberg, I. Mandel, R. O'Shaughnessy, M. Pitkin, C. Rodriguez, C. Röver, T. Sidery, R. Smith, M. Van Der Sluys, A. Vecchio, W. Vousden, and L. Wade. Parameter estimation for compact binaries with ground-based gravitational-wave observations using the LALInference software library. *Physical Review D*, 91(4), feb 2015.

[18] Nelson Christensen and Renate Meyer. Parameter estimation with gravitational waves. *Rev. Mod. Phys.*, 94(2):025001, 2022.

[19] B. S. Sathyaprakash and Bernard F. Schutz. Physics, astrophysics and cosmology with gravitational waves. *Living Reviews in Relativity*, 12(1), mar 2009.

[20] Emily Baird, Stephen Fairhurst, Mark Hannam, and Patricia Murphy. Degeneracy between mass and spin in black-hole-binary waveforms. *Phys. Rev. D*, 87(2):024035, 2013.

[21] Gilles Esposito-Farese. Binary pulsar tests of strong field gravity and gravitational radiation damping. In *10th Marcel Grossmann Meeting on Recent Developments in Theoretical and Experimental General Relativity, Gravitation and Relativistic Field Theories (MG X MMIII)*, pages 647–666, 2 2004.

[22] R A Hulse and J H Taylor. Discovery of a pulsar in a binary system. *Astrophys. J., Lett., v. 195, no. 2, pp. L51-L53*, 1 1975.

[23] M. Kramer et al. Strong-Field Gravity Tests with the Double Pulsar. *Phys. Rev. X*, 11(4):041050, 2021.

[24] Joel M. Weisberg and Yuping Huang. Relativistic Measurements from Timing the Binary Pulsar PSR B1913+16. *Astrophys. J.*, 829(1):55, 2016.

[25] M. Kramer, I. H. Stairs, R. N. Manchester, N. Wex, A. T. Deller, W. A. Coles, M. Ali, M. Burgay, F. Camilo, I. Cognard, T. Damour, G. Desvignes, R. D. Ferdman, P. C. C. Freire, S. Grondin, L. Guillemot, G. B. Hobbs, G. Janssen, R. Karuppusamy, D. R. Lorimer, A. G. Lyne, J. W. McKee, M. McLaughlin, L. E. Münch, B. B. P. Perera, N. Pol, A. Possenti, J. Sarkissian, B. W. Stappers, and G. Theureau. Strong-field gravity tests with the double pulsar. *Phys. Rev. X*, 11:041050, Dec 2021.

[26] Abhirup Ghosh. Summary of Tests of General Relativity with GWTC-3. In *56th Rencontres de Moriond on Gravitation*, 4 2022.

[27] 116(22), may 2016.

[28] Gravitational waves and gamma-rays from a binary neutron star merger: GW170817 and GRB 170817a. *The Astrophysical Journal*, 848(2):L13, oct 2017.

[29] Tests of general relativity with gw170817. Jul 2019.

[30]

[31] Pankaj Saini, Marc Favata, and K. G. Arun. Systematic bias on parametrized tests of general relativity due to neglect of orbital eccentricity. *Phys. Rev. D*, 106:084031, Oct 2022.

[32] Marc Favata. Systematic parameter errors in inspiraling neutron star binaries. *Phys. Rev. Lett.*, 112:101101, Mar 2014.

[33] Paul D. Lasky, Eric Thrane, Yuri Levin, Jonathan Blackman, and Yanbei Chen. Detecting gravitational-wave memory with LIGO: implications of GW150914. *Phys. Rev. Lett.*, 117(6):061102, 2016.

[34] Miriam Cabero, Alex B. Nielsen, Andrew P. Lundgren, and Collin D. Capano. Minimum energy and the end of the inspiral in the post-newtonian approximation. *Physical Review D*, 95(6), mar 2017.